Planar folding of shallow tape springs: The rod model with flexible cross-section revisited as a regularized Ericksen bar model

M. Martin, Stéphane Bourgeois, B. Cochelin, F. Guinot

Planar folding of shallow tape springs: the rod model with flexible cross-section revisited as a regularized Ericksen bar model.

M. Martin[a,b], S. Bourgeois[a,*], B. Cochelin[a], F. Guinot[b]

[a] *Aix-Marseille Univ, CNRS, Centrale Marseille, LMA UMR 7031, Marseille, France*
[b] *Thales Alenia Space, Cannes La Bocca, France*

Abstract

This work concerns the parallel that can be made between two models involving propagating instabilities: (1) a reguralized Ericksen bar model and (2) a rod model with flexible cross-section dedicated to the folding of tape springs. This comparison confirms and complements the estimates obtained by Seffen and Pellegrino (1999) and gives some new insights on the formation and growth of folds, including their number and their location. We begin by studying a reguralized Ericksen bar model in statics. The complete bifurcation diagram is analyzed, together with the post-buckling deformed shapes. The influence of the reguralization parameter and of the boundary conditions is also studied. Then we propose a simplified model derived from Guinot et al. (2012) and Picault et al. (2014) to account for the folding of shallow tape springs in opposite sense bending. The equations that govern

*Corresponding author. Tel.: +33 484524259.
Email addresses: martin@lma.cnrs-mrs.fr (M. Martin), stephane.bourgeois@centrale-marseille.fr (S. Bourgeois), bruno.cochelin@centrale-marseille.fr (B. Cochelin), francois.guinot@thalesaleniaspace.com (F. Guinot)

the problem, involving only two kinematic variables, can be easily written in this case. An analytical expression is found for the fundamental solution that is characteristic of an Ericksen bar model and it is shown that higher order terms that appear in the strain energy account for the transition zones. The obvious parallel with a reguralized Ericksen bar model is made by proceeding to a complete study of the post-bifurcation diagram. Estimates of the length of the transition zones are proposed and compared to those obtained with a FE shell model. A FE shell model is also used to validate the fundamental solution obtained with the proposed simplified rod model with flexible cross-section. These comparisons lead to good agreements, except for the peak moment of the moment-curvature response for the bending test. An enriched model is then proposed that brings significant improvements.
Keywords: Non-linear rod model, Tape spring, Folding, Reguralized Ericksen bar, Flexible cross-section.

1. Introduction

One usually knows tape springs as measuring tools but these very slender and thin curved structures show some interesting behaviours commonly used in other engineering fields. For example, tape springs are of special interest to deploy systems in spatial engineering because of their lightness and compactness in folded or coiled configuration: some telescopes, reflectors or masts (Black et al., 2006; Pellegrino, 2002; Murphey et al., 2010) are composed of tape springs. Due to some unique behaviours, tape springs already constitute solutions for autonomous and reliable deployable structures when employed as hinges to link two other rigid parts, as the MAEVA hinge

(Donzier and Sicre, 1997).

One of the most important issue is to correctly model the behaviour of these elastic structures which are subject to buckling and propagating instabilities in the framework of large displacements (Wuest, 1954; Seffen and Pellegrino, 1999). Regarding the geometry of tape springs, one can choose to use a shell model and solve it with the finite element method (Seffen et al., 2000; Hoffait et al., 2010; Walker and Aglietti, 2007; Soykasap, 2012). This approach seems to be the most accurate but these shell finite element models have to be carried out by experts due to the complexity of the behaviour of such structures. In this context, simpler models based on rigid bars and rotational spring, have been established in some specific cases (Seffen and Pellegrino, 1999). However, these models are not able to account for the creation, splitting or merging of folds (folds are introduced *ab initio*) and are restricted to planar motion in the plane of symmetry of the tape (no transverse bending nor twisting). More recently, Guinot et al. (2012) have proposed a planar rod model with flexible cross-section, which is able to account for the complete flattening of the cross-section in the fold regions. This model was improved by Picault et al. (2014) and an extension to 3D motions including torsion is proposed in Picault et al. (2016). These works have led to a family of models which are able to account for complex scenarios of 3D foldings, involving bending and twisting as well as the creation of folds, their migration along the tape and their duplication. This family of models will be referred to henceforth as *RFleXS* models (for *Rods with Flexible X-Section*).

The understanding of the phenomena that lead to the formation and

growth of localized folds was addressed by Seffen and Pellegrino (1999). These authors are referring to the work of Wuest (1954) who has studied the behaviour of a tape-spring under uniform longitudinal bending. In this work, an analytical solution is found for the bending moment with respect to the prescribed (uniform) curvature, which follows an up-down-up law. Seffen and Pellegrino (1999) explain that this property is the key feature that leads to the formation and growth of localized folds. A parallel is made with a class of problems called *propagating instabilities* (Kyriakides, 1993) and a qualitative comparison with the propagation of bulges during the inflation of rubber balloons is shown. This parallel suggests useful methods that can be used to estimate some overall mechanical properties of folded tape-springs (longitudinal curvature in the fold area, propagating fold moment...). But it does not explain the particularities of the overall response $M(\theta)$ which exhibits an hysteretic behaviour when the rotations of the cross-sections $\pm\theta$ at ends (M is the bending moment) are prescribed. The model does not predict the location of folds and the crucial role of the transition zones between the fold and the almost undeformed parts.

The problem is revisited here by referring to a reguralized Ericksen bar model. Ericksen (1975, 1998) has studied the tensile test of a bar with a non-convex strain energy density, which leads to an up-down-up constitutive law. He has shown that for a range of prescribed displacements, solutions that realize an absolute minimum of the potential energy correspond to a piecewise two-phase bar. He has also shown that for this range of prescribed displacements, the stress remains the same and the overall response exhibits a plateau. But the model does not predict the location of the two phases

(only the volume fractions are determined) and strain jumps are introduced at the interfaces of the phases. In litterature, the problem is typically reguralized by adding a term to the strain energy that depends on the strain gradient. As many authors (Carr et al., 1984; Truskinovsky and Zanzotto, 1996; Rogers and Truskinovski, 1997; Puglisi and Truskinovsky, 2002), we consider an additional term that is quadratic with respect to the strain gradient. The problem is then reguralized in the sense that the formation of regions with rapid changes in strain is penalized (Truskinovsky and Zanzotto, 1996). With this additional term in the strain energy, solutions now exhibit transition zones between the two different phases (instead of strain jumps) and it eliminates uncertainties about the location of the phases.

In this paper, a *RFleXS* model dedicated to the pure opposite-sense bending test of shallow tape-springs is proposed, based on the previous works of Guinot et al. (2012) and Picault et al. (2014). The analysis of this approximate 1D-model allows to make a parallel with a reguralized Ericksen bar model. It leads to a deep understanding of the principles that govern the formation and growth of folds. We obtain the same hysteretic behaviour for the two models. This comparison also confirms and complements the estimates obtained by Seffen and Pellegrino (1999) for the overall mechanical key features.

Similarities can be found here with the problem of necking of elastic bars in tension. For instance, Coleman and Newman (1988) show that an ansatz-based kinematics leads to a reguralized 1D Ericksen bar model that can explain strain localization phenomena in slender bars. More recently, Audoly and Hutchinson (2016) have derived rigorous models based on asymp-

totic analysis. An exhaustive review on this topic can be found in this reference. The proposed approximate 1D model is here derived from a non-linear shell theory by introducing additional kinematics assumptions and addresses the folding of tape-spring ribbons, due to curvature localization phenomena.

The paper is organized as follows. Section 2 is devoted to preliminary results obtained for the behaviour in statics of a classical reguralized Ericksen bar model. Bifurcation diagrams are examined in depth and it is shown that boundary conditions prescribed on higher order terms are of great influence. When von-Neumann conditions are considered, the bifurcation diagram exhibits a finite number of loops connected in two points to the fundamental branch.

Section 3 recalls the main ideas underlying the planar rod model with flexible cross-section (Guinot et al., 2012; Picault et al., 2014) and a model dedicated to the pure opposite-sense bending test of shallow tape-springs is proposed. In this case, the *RFleXS* model only involves two kinematic variables and strong form expressions of the governing equations can be obtained. Non-dimensionalization of the equations shows that the behaviour is mainly governed by the Batdorf parameter and the ratio between the width of the tape-spring and its length.

Section 4 adresses the link between the reguralized Ericksen bar model and the simplified rod model with flexible cross-section. These two models exhibit the same properties for the bifurcation diagrams, that depend on the prescribed boundary conditions on higher order terms. In the *RFleXS* model, these higher order terms govern the length of the transition zones. Estimates of this length are proposed and compared to results obtained with FE shell

models.

Section 5 is devoted to the comparison between the *RFleXS* model and shell models. The *RFleXS* model is first compared with the analytical model of Wuest (1954), and then with FE shell models. These comparisons lead to good agreements, except for the peak moment of the moment-rotation response for the bending test. An enriched model is then proposed that brings significant improvements.

2. The reguralized Ericksen bar model

2.1. The Ericksen bar model

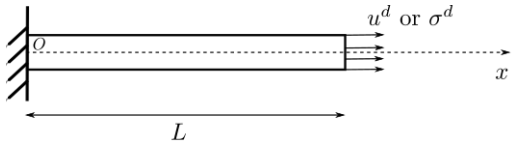

Figure 1: Uniaxial problem of the bar

Let us consider the uniaxial tension of an elastic bar as shown in Figure 1. The axial displacement, strain and stress are denoted by $u(x)$, $\varepsilon(x)$ and $\sigma(x)$ respectively, with $\varepsilon = u' = \frac{\mathrm{d}u}{\mathrm{d}x}$. A non-convex potential $u_e(\varepsilon)$ is considered (Ericksen, 1975, 1998), such that the constitutive behaviour given by $\sigma = \frac{\mathrm{d}u_e}{\mathrm{d}\varepsilon}$ follows an up-down-up response as shown in Figure 2 (right).

More precisely, we assume the following properties :

- the strain energy $u_e(\varepsilon)$ is of class $\mathbf{C}^{(3)}$,
- for $\varepsilon < \varepsilon_1$ and $\varepsilon > \varepsilon_2$, $\frac{\mathrm{d}\sigma}{\mathrm{d}\varepsilon} = \frac{\mathrm{d}^2 u_e(\varepsilon)}{\mathrm{d}\varepsilon^2} > 0$,

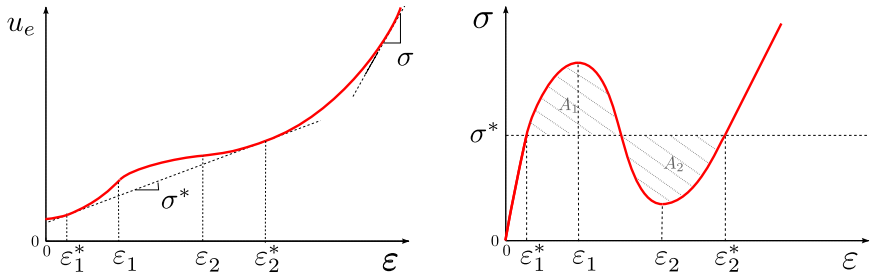

Figure 2: Left: strain energy density $u_e(\varepsilon)$ of the Ericksen bar model. Right: corresponding up-down-up response $\sigma(\varepsilon)$ and illustration of the Maxwell equal area rule for the determination of the *Maxwell stress* σ^*.

- for $\varepsilon_1 < \varepsilon < \varepsilon_2$, $\frac{\mathrm{d}\sigma}{\mathrm{d}\varepsilon} = \frac{\mathrm{d}^2 u_e(\varepsilon)}{\mathrm{d}\varepsilon^2} < 0$ and $\frac{\mathrm{d}^2\sigma}{\mathrm{d}\varepsilon^2} = \frac{\mathrm{d}^3 u_e(\varepsilon)}{\mathrm{d}\varepsilon^3} < 0$,
- $\frac{\mathrm{d}\sigma}{\mathrm{d}\varepsilon}(\varepsilon_1) = \frac{\mathrm{d}\sigma}{\mathrm{d}\varepsilon}(\varepsilon_2) = 0$.

The bar is clamped at left end $x = 0$. At right end $x = L$, two cases may be considered: prescribed displacement u^d or prescribed stress σ^d. We first consider a prescribed stress. The problem is then governed by the following equations:

$$\begin{aligned} &\sigma' = 0,\ \sigma = \frac{\mathrm{d}u_e}{\mathrm{d}\varepsilon}, \varepsilon = u', \\ &u(0) = 0 \text{ and } \sigma(L) = \sigma^d. \end{aligned} \tag{1}$$

Equilibrium conditions lead to a uniform stress along the bar $\sigma(x) = \sigma^d$, but depending on the value of σ^d, there is up to three solutions for the strain. Considering that jumps of strains are allowed, Figure 3 depicts the set of equilibrium solutions in the plot of the applied stress $\sigma = \sigma^d$ with respect to the normalized displacement at right end (the average strain): $\frac{u(L)}{L} = \frac{1}{L}\int_0^L \varepsilon \,\mathrm{d}x = \langle\varepsilon\rangle$. For a couple $(\langle\varepsilon\rangle, \sigma)$ in the grey area or on the up-down-up curve, there is at least one distribution of strains $\varepsilon(x)$ that satisfies

the equations (1) of the problem. But unstable, metastable (local minima of the elastic potential energy) and stable (absolute minima) solutions may be distinguished. Stable solutions are plotted in red lines in Figure 3 and correspond to homogeneous distribution of strains (Ericksen, 1998). For a given stress $\sigma = \sigma^d$, strains that realize the absolute minima of the elastic potential energy are the ones for which the tangent remains under the strain energy for all strains in Figure 2. For one value of σ, there is only one value of strain ε that realizes that minimum except for the value of the stress $\sigma = \sigma^*$ (the Maxwell stress) for which there are two solutions ε_1^* and ε_2^*. A graphical analysis of the left plot in Figure 2 leads to:

$$\sigma^*(\varepsilon_2^* - \varepsilon_1^*) = u_e(\varepsilon_2^*) - u_e(\varepsilon_1^*) = \int_{\varepsilon_1^*}^{\varepsilon_2^*} \frac{\mathrm{d}u_e}{\mathrm{d}\varepsilon}\,\mathrm{d}\varepsilon = \int_{\varepsilon_1^*}^{\varepsilon_2^*} \sigma(\varepsilon)\,\mathrm{d}\varepsilon.$$

It shows that the stress σ^* and the strains ε_1^* and ε_2^* obey the Maxwell equal area rule: the hatched areas A_1 and A_2 are equal in the plot of the corresponding constitutive law in Figure 2 (right).

Figure 4 shows the response when a displacement u^d is applied at right end instead of a stress σ^d. The average strain $\langle\varepsilon\rangle = u^d/L$ is then prescribed in this case. The up-down-up curve and the grey area depict again the set of equilibrium solutions. The thick red line refers to the plot of the stress σ that realizes the absolute minimum of the potential strain energy for a prescribed average strain $\langle\varepsilon\rangle$ (Ericksen, 1975, 1998). For $\langle\varepsilon\rangle \leq \varepsilon_1^*$ and $\langle\varepsilon\rangle \geq \varepsilon_2^*$, the strain is uniform along the bar. For $\varepsilon_1^* < \langle\varepsilon\rangle < \varepsilon_2^*$, the uniform solution is not the solution that minimizes the potential strain energy. In this regime, the stress equals the Maxwell stress and the distribution of strains consists in a two-phase bar with a fraction α_1 at strain ε_1^* and a fraction $\alpha_2 = 1 - \alpha_1$ at strain ε_2^*, such that $\alpha_1\,\varepsilon_1^* + \alpha_2\,\varepsilon_2^* = \langle\varepsilon\rangle$, the applied average strain. For a

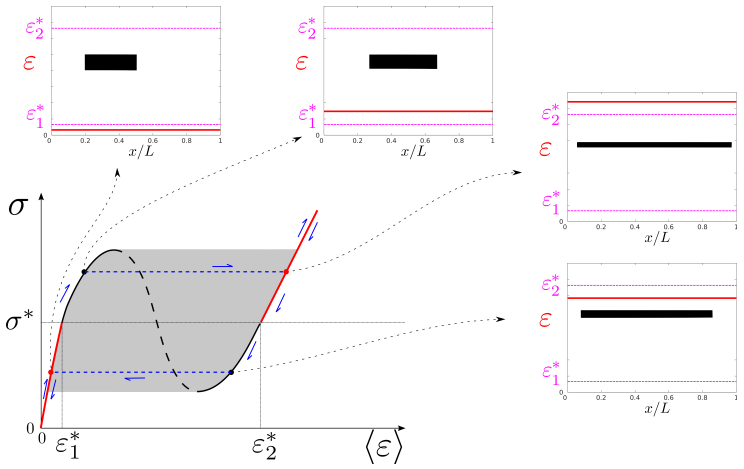

Figure 3: Stress - average strain curve of the Ericksen bar for a prescribed stress $\sigma = \sigma^d$. Set of equilibrium solutions (up-down-up curve and grey area). Stable solutions in red (absolute minima of the potential energy). Metastable (resp. unstable) homogeneous solutions in black line (resp. black dashed line). Illustration of a loading-unloading scenario (in blue): when a bar shifts from a homogeneous metastable solution, it commonly jumps to a configuration corresponding to the lowest potential energy. In boxes: strain distribution in the bar. The black icons are schematic illustrations of the deformed shapes of the bar.

prescribed average strain between ε_1^* and ε_2^*, the model does not predict the number of phase transitions and their locations but only the volume fraction of the two phases. There is an infinity of solutions for the location of the two phases along the bar. Jumps of strains are allowed and can occur anywhere since no energy is associated with the strain gradient, which often disagrees with observations.

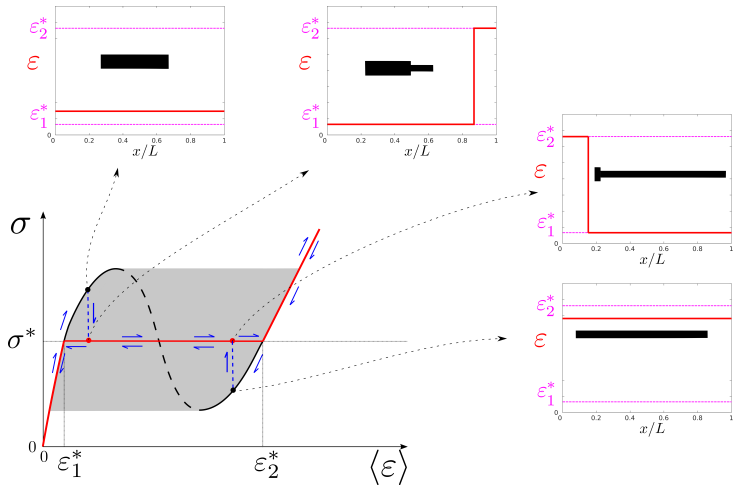

Figure 4: Stress - average strain curve of the Ericksen bar for a prescribed normalized displacement $\langle\varepsilon\rangle = u^d/L$. Set of equilibrium solutions (up-down-up curve and grey area) . Stable solutions in red (absolute minima of the potential energy). Metastable (resp. unstable) homogeneous solutions in black line (resp. black dashed line). Illustration of a loading-unloading scenario (in blue): when a bar shifts from a homogeneous metastable solution, it commonly jumps to a configuration corresponding to the lowest potential energy. In boxes: strain distribution in the bar, assuming only one phase transition (jump of strain). The black icons are schematic illustrations of the deformed shapes of the bar (thick and thin parts corresponding to small and large longitudinal strain, respectively).

2.2. The reguralized Ericksen bar model

The problem can be reguralized by introducing a penalization for the formation of interfaces. The simplest way is to consider a dependence of the strain energy on the higher derivatives of the displacement, which can be justified in some cases by an asymptotic analysis (Audoly and Hutchinson, 2016). As many authors (Carr et al., 1984; Truskinovsky and Zanzotto, 1996; Rogers and Truskinovski, 1997; Puglisi and Truskinovsky, 2002), we consider

an additional term to the strain energy which is quadratic with respect to the second derivative of the displacement: $u_r(u) = \frac{1}{2}\alpha u''^2$ with $\alpha > 0$. The problem is then reguralized in the sense that the formation of regions with rapid changes in strain is penalized (Truskinovsky and Zanzotto, 1996). It leads to the appearence of transition zones with a given length between the two phases and to a bounded number of transition zones along the bar. Truskinovsky and Zanzotto (1996) propose an approach to study such a regularized Ericksen bar under elastic foundation: the transition zones are considered as interfaces and the number of interfaces and their positions are considered as variables. For a fixed number of interfaces, they search for the local minimizers of the energy with respect to the positions of the interfaces. In the following, we address the problem by the way of a bifurcation analysis.

2.3. Linear buckling analysis of the reguralized Ericksen bar model

Let us consider the reguralized problem with prescribed displacements at ends $u(0) = 0$ and $u(L) = u^d$. Considering the strain energy density $u_e + u_r$, the strong form of the problem can be written:

$$\begin{gathered} \sigma' = 0,\ \sigma = \frac{\mathrm{d}u_e}{\mathrm{d}\varepsilon} - \alpha\varepsilon'', \varepsilon = u', \\ u(0) = 0,\ u(L) = u^d, \\ + \text{ conditions on } u'(0) \text{ (or } \alpha u''(0)) \text{ and } u'(L) \text{ (or } \alpha u''(L)). \end{gathered} \tag{2}$$

One can notice that new boundary conditions are required, due to the presence of higher order terms in the strain energy density. We consider that strains $\varepsilon = u'$ are free at ends, which means that the associated forces vanish :

$$\alpha u''(0) = \alpha u''(L) = 0. \tag{3}$$

The fundamental solution of the problem (2) with (3) is obtained for a uniform strain and stress state, obeying the up-down-up curve plotted in Figure 2:

$$u_u(x) = \frac{u^d}{L}x,\ \varepsilon_u = \frac{u^d}{L} \text{ and } \sigma_u = \tfrac{\mathrm{d}u_e}{\mathrm{d}\varepsilon}(\varepsilon_u). \tag{4}$$

A linear buckling analysis is then performed. We search for $u = u_u + \Delta u$, $\varepsilon = \varepsilon_u + \Delta\varepsilon$ and $\sigma = \sigma_u + \Delta\sigma$ verifying the problem (2) with (3). Considering Δu, $\Delta\varepsilon$ and $\Delta\sigma$ as small perturbations, the following first order system is found:

$$\begin{aligned} &\tfrac{\mathrm{d}^2u_e}{\mathrm{d}\varepsilon^2}(\varepsilon_u)\Delta u'' - \alpha\Delta u'''' = 0, \\ &\Delta u(0) = \Delta u''(0) = \Delta u(L) = \Delta u''(L) = 0. \end{aligned} \tag{5}$$

If $\frac{\mathrm{d}^2u_e}{\mathrm{d}\varepsilon^2}(\varepsilon_u) \geq 0$, equations (5) only admit the trivial solution $\Delta u(x) = 0$. If $\frac{\mathrm{d}^2u_e}{\mathrm{d}\varepsilon^2}(\varepsilon_u) < 0$, the non trivial solutions $\Delta u_k(x) = D_k \sin\left(\frac{k\pi x}{L}\right)$ are obtained for $\varepsilon_u = \varepsilon_k^b$ such that:

$$\frac{\mathrm{d}^2u_e}{\mathrm{d}\varepsilon^2}(\varepsilon_k^b) = -\alpha k^2\frac{\pi^2}{L^2},\ \text{with } k \in \mathbb{N}^*. \tag{6}$$

The right-hand side of equation (6) is strictly negative and $\frac{\mathrm{d}^2u_e}{\mathrm{d}\varepsilon^2}(\varepsilon) = \frac{\mathrm{d}\sigma_u}{\mathrm{d}\varepsilon}(\varepsilon)$ is the slope at abscissa ε of the up-down-up curve shown Figure 2 (right). Solutions are then searched in the decreasing part of this curve, *i.e.* for $\varepsilon \in]\varepsilon_1, \varepsilon_2[$. Figure 5 illustrates a graphical way of finding the bifurcation points. Assuming that $-\frac{\mathrm{d}\sigma_u}{\mathrm{d}\varepsilon}(\varepsilon)$ is of class $\mathbf{C}^{(2)}$ and strictly convex for $\varepsilon \in]\varepsilon_1, \varepsilon_2[$, $-\frac{\mathrm{d}\sigma_u}{\mathrm{d}\varepsilon}(\varepsilon)$ is bell-shaped in this interval. The solution ε_k^b are the abscissas of

the intersection points of the curve $-\frac{\mathrm{d}\sigma_u}{\mathrm{d}\varepsilon}(\varepsilon)$ and the horizontal lines located at ordinates $\alpha k^2 \frac{\pi^2}{L^2}$ for $k \in \mathbb{N}^*$. Since $-\frac{\mathrm{d}\sigma_u}{\mathrm{d}\varepsilon}(\varepsilon)$ is bell-shaped and upper bounded, it leads to a finite number of bifurcation points that can be grouped in pairs for which the linear buckling mode is the same. The abscissas of the intersection points are then redenoted by ε_k^A and ε_k^B.

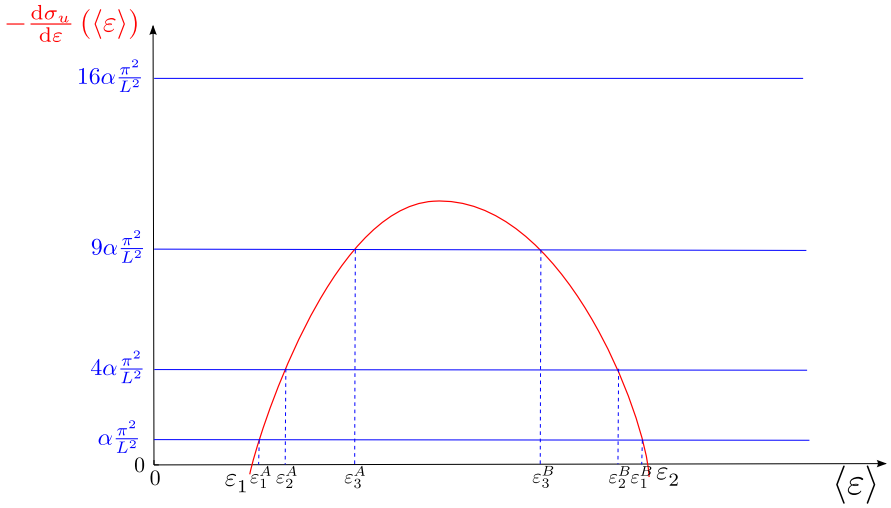

Figure 5: Schematic graphical determination of the bifurcation points for the reguralized Ericksen bar model: the critical average strains are the abscissas of the intersection points of the curve $-\frac{\mathrm{d}\sigma_u}{\mathrm{d}\varepsilon}(\varepsilon)$ and the horizontal lines located at ordinates $\alpha k^2 \frac{\pi^2}{L^2}$.

2.4. Post-buckling analysis of the reguralized Ericksen bar model

The goal of this section is to illustrate the links between the linear buckling mode shapes and the post-buckling shapes which tend to a two-phase bar with transition zones at different locations. The post-buckling analysis cannot be done with a general form of the strain energy and the following academic example is considered:

$$u_e(\varepsilon) = \frac{9}{4}\varepsilon^2 - \varepsilon^3 + \frac{1}{8}\varepsilon^4.$$

This example has the advantage to lead to simple expressions of the key features listed in Table 1.

σ^*	ε_1^*	ε_2^*	ε_1	ε_2	$\sigma(\varepsilon_1)$	$\sigma(\varepsilon_2)$
1	$2-\sqrt{3}$	$2+\sqrt{3}$	1	3	2	0

Table 1: Key features for the Ericksen bar model.

The resulting up-down-up response $\sigma_u(\varepsilon)$ of the associated Ericksen bar is shown Figure 6. The linear buckling analysis with a reguralization parameter α/L^2=5e-3 is also presented in this figure. Ten bifurcation points are found in the decreasing part of the curve $\sigma_u(\varepsilon)$ and the five associated linear buckling mode shapes are given by $\Delta u_k(x) = D_k \sin\left(\frac{k\pi x}{L}\right)$ with $k = 1, ..., 5$.

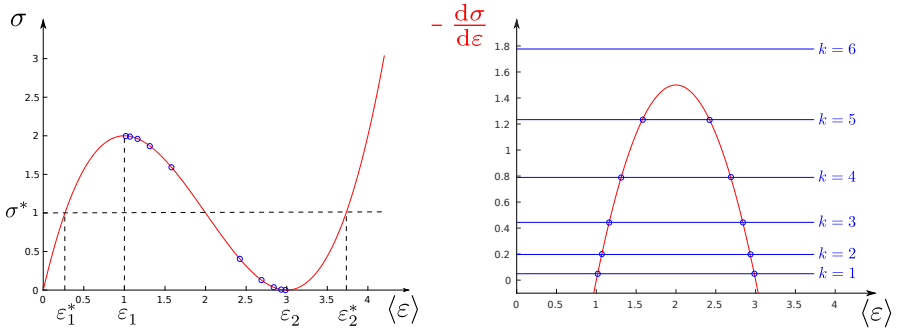

Figure 6: Up-down-up curve $\sigma_u(\langle\varepsilon\rangle)$ of the Ericksen bar model with bifurcation points (left) and graphical determination of these bifurcation points (rights): the critical strains are the abscissas of the intersection points of the curve $-\frac{d\sigma_u}{d\varepsilon}(\langle\varepsilon\rangle)$ and the horizontal lines at ordinates $\alpha k^2 \frac{\pi^2}{L^2}$ $(\alpha/L^2 = 5e-3)$.

A post-bifurcation analysis has been performed with the software ManLab-4.0 (2018), which is based on the path-following Asymptotic Numerical Method with an automatic detection of bifurcation points. The displacement $u(x)$ is discretized by the finite element method with a third-order Hermite interpolation. The bifurcation diagram in the plane $(\langle\varepsilon\rangle, \sigma)$ is presented in Figure 7 (top left), for α/L^2=5e-3. Locations of bifurcation points are in agreement with those obtained with the linear buckling analysis. This diagram shows that bifurcation points with the same linear buckling mode shape are connected by a post-bifurcation branch. The bifurcation diagram in the plane $(\langle\varepsilon\rangle, \varepsilon(L))$ at the top-right of Figure 7 shows that each branch k is in reality a loop. In this plane, the fundamental branch coincides with the first bisector since the strain distribution is uniform. Points A_k and B_k split each loop k in two half-loops $k(a)$ and $k(b)$. The two half-loops $k(a)$ and $k(b)$ can be associated with two different post-buckling deformed shapes with the same number k of transition zones separating extrema of strains, but they differ in the locations of these extrema (see the boxes at the bottom of Figure 7). The two half-loops of each branch k in the plane $(\langle\varepsilon\rangle, \sigma)$ appears to be superposed (see top left plot in Figure 7) and present a plateau at the value of the Maxwell stress σ^* when the number of transition zones is small (for k=1 and 2 in Figure 7). In this case, the aggregated length of transition zones compared to the total length of the bar is sufficiently small to allow the formation of areas with uniform distributions of strains ε_1^* and ε_2^* (see Figure 7: boxes at the bottom and bifurcation diagram at top right).

Figure 8 illustrates the evolution of the post-bifurcation shape along the

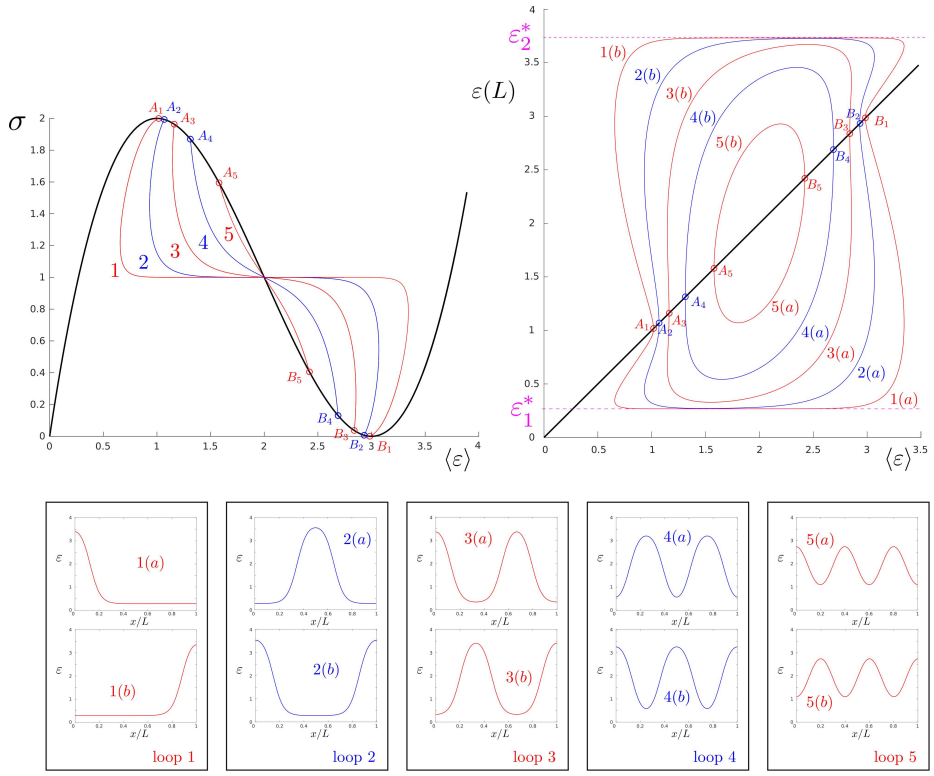

Figure 7: Tensile test for the reguralised Ericksen bar with $\alpha/L = 5e-3$. Top left: bifurcation diagram in the plane $(\langle\varepsilon\rangle, \sigma)$. Top right: bifurcation diagram in the plane $(\langle\varepsilon\rangle, \varepsilon(L))$. Each post-bifurcation branch is in reality a loop. Points A_k and B_k split each loop k in two half-loops $k(a)$ and $k(b)$. The two half-loops $k(a)$ and $k(b)$ can be associated with two different post-buckling deformed shapes with the same number k of transition zones separating extrema of strains, but they differ in the locations of these extrema. In boxes: distribution of strains along the bar for each half-loop, at the beginning of the plateau for loops 1,2 and 3 and near $\langle\varepsilon\rangle = 2$ for loops 4 and 5.

first loop. At point A_1, the strain distribution is uniform along the bar and equal to ε_1^A. The linear buckling analysis leads to a strain perturbation $\Delta\varepsilon_1(x) = D_1 \frac{\pi}{L} \cos\left(\frac{\pi x}{L}\right)$. The two half-loops $1(a)$ and $1(b)$ starting from A_1

correspond to the two possibilities for the sign of the constant D_1, which inverts the locations of the minimum and the maximum of strains. Moving from A_1 to B_1 along the half-loops, three parts can be distinguished. The first part between A_1 and the plateau corresponds to the formation of a peak of strain at the initial location of the maximum: at the left end for the half-loop 1(a) and at the right end for the half-loop 1(b). At the beginning of the plateau, the strain distribution presents a peak equal to ϵ_2^* at one end, a transition zone and a large zone at uniform strain ϵ_1^*. On the plateau, the transition zone moves along the bar and the zone at strain ϵ_2^* propagates whereas the zone at strain ϵ_1^* shortens. At the end of the plateau, the strain distribution presents a large part at uniform strain ϵ_2^*, a transition zone and an inverted peak equal to ϵ_1^* located at the opposite end of the bar. The part between the end of the plateau and the point B_1 corresponds to the disappearance of the inverted peak at end which leads to a uniform strain distribution equal to ε_1^B at point B_1. Similar scenarios are obtained for the other branches k that exhibit a plateau: starting from A_k, the uniform distribution of strains degenerates to form parts at uniform strain ϵ_1^* and peaks at the value ϵ_2^*, the locations of which are governed by the linear buckling mode. On the plateau, the transition zones move along the bar and parts at ϵ_2^* propagate whereas parts at strain ϵ_1^* shorten. At the end of the plateau, the strain distribution exhibits parts at uniform strain ϵ_2^* and inverted peaks at strain ϵ_1^*. Between the end of the plateau and the point B_k, we observe the disapearence of the inverted peaks which lead to a uniform distribution of strains.

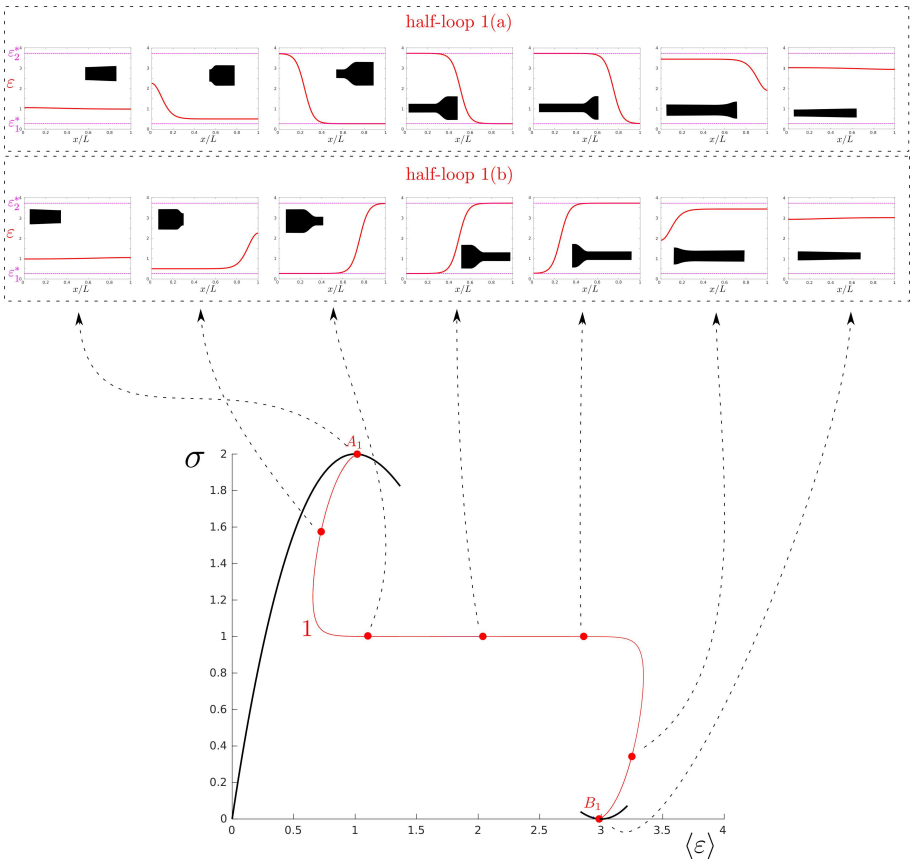

Figure 8: Evolution of the strain distribution in the bar on the first bifurcation branch. The black icons are schematic illustrations of the deformed shapes of the bar (thin and thick parts corresponding to small and large longitudinal strain, respectively). From A_1 to B_1, we observe a strain localization at one end that propagates along the bar.

2.5. Influence of the boundary conditions and the reguralization parameter

The analysis has been conducted for a prescribed displacement at the right end of the bar: $u(L) = u^d$. The same analysis can be done with a prescribed stress $\sigma(L) = \sigma^d$ and leads to the same results for the bifurcation diagrams. As above mentioned, additional boundary conditions have been

required due to the presence of the reguralization term in u'' in the strain energy. The choice of strain free condition at ends have been adopted for the above analyses: $u''(0) = u''(L) = 0$. If Dirichlet conditions are considered ($u'(0) = u'(L) = 0$), the problem is completely different: the uniform distribution of strains is no more a solution of the problem. Figure 9 compares the bifurcation diagrams obtained for the two cases of boundary conditions for two values of the reguralization parameter α/L^2. The bifurcation diagram in black lines corresponds to the von-Neumann boundary conditions $u''(0) = u''(L) = 0$ and the curve in red is obtained with the Dirichlet boundary conditions $u'(0) = u'(L) = 0$. The Dirichlet conditions act as a perturbation to the problem with von-Neumann conditions. There are no more bifurcation points and the response tends to follow some particular branches. The response is very close to the fundamental branch at the beginning and turns quite smoothly to follow a branch of the second loop. This branch corresponds to the half-loop $2(a)$ in Figure 7, which is the first bifurcated branch for which the strain distribution in the bar is the "more compatible" with the Dirichlet boundary conditions $\varepsilon(0) = \varepsilon(L) = 0$ (see boxes at the bottom of Figure 7). The response follows the plateau and then goes up and tends to join the fundamental response obtained with the von-Neumann conditions (uniform distribution of strains). This scenario is more obvious when the reguralization parameter α/L^2 is smaller. In this case, the length of the transition zones is smaller. More bifurcation branches are found and the perturbation due to Dirichlet conditions instead of von-Neumann ones is smaller.

The deformed shape of the bar on the plateau is shown on Figure 9. A

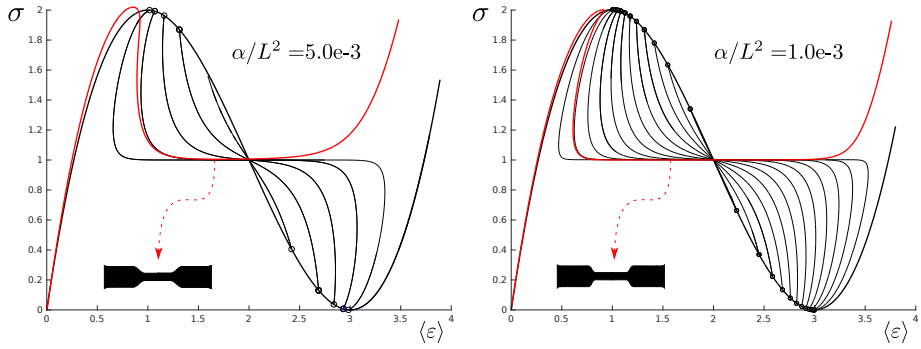

Figure 9: Comparison of the bifurcation diagrams obtained with von-Neumann (in black) and Dirichlet boundary conditions (red) on the higher order terms for two values of the reguralization parameter. Black icons : Schematic deformed shape of the bar (thin and thick parts corresponding to large and small longitudinal strain, respectively)

strain localization appears in the middle. It leads to a two-phase bar with a middle part at strain ε_2^* connected to two parts at strain ε_1^* with transition zones. We also observe small edge effects at the boundaries because of the imposed zero strain. On the plateau, when the average strain $\langle\varepsilon\rangle$ increases, the transition zones move along the bar. The middle part at strain ε_2^* grows whereas the parts at strain ε_1^* shortens.

A parallel can be made with the bending of tape-springs in opposite sense. If the cross-sections are maintained rigid at ends, a fold occurs in the middle of the tape and grows at constant moment until the fold occupies the entire length of the tape. The curve of the bending moment versus the prescribed rotation follows the same shape as the red curves shown in Figure 9. The parallel between the behaviour of a reguralized Ericksen bar and the bending behaviour of a tape-spring can be clearly established by using the rod model with flexible cross-section. In the following, a rod model dedicated

to opposite-sense bending of shallow tape springs is derived from the works of Guinot et al. (2012) and Picault et al. (2014).

3. The bending rod model with flexible cross-section for shallow tape-springs

3.1. Kinematic description

The tape spring is seen in its initial configuration as a shell that resembles a thin-walled beam with an arc-of-circle cross-section. The middle surface of the shell results from the orthogonal extrusion of an arc-of-circle along a unit vector $\boldsymbol{e_1}$ (see Figure 10). Let O be the centroid of the extruded arc-of-circle. The unit vector $\boldsymbol{e_3}$ is chosen such that the plane $(O, \boldsymbol{e_1}, \boldsymbol{e_3})$ is the tape spring plane of symmetry (with $\boldsymbol{e_3}$ oriented towards the centroids, as shown in Figure 10). The last unit vector $\boldsymbol{e_2}$ is created to form the fixed direct orthonormal system $(\boldsymbol{e_1}, \boldsymbol{e_2}, \boldsymbol{e_3})$. One can remark that axis $(O, \boldsymbol{e_1})$ contains the centerline of the tape-spring when considered as a thin-walled beam in the undeformed configuration.

In the following, the cross-section curve refers to the intersection of the middle surface of the shell and the cross-section plane. The cross-section curve is initially an arc-of-circle of radius R_0 and of half-length a. The longitudinal length of the tape spring is denoted by L. The shell middle surface is parametrized by the curvilinear abscissas $(s_1, s_2) \in [0, L] \times [-a, a]$ (s_1 in the longitudinal direction and s_2 in the transverse one).

Only the static case in the framework of a planar motion is studied. In order to reduce the shell model into a rod model with flexible cross-section,

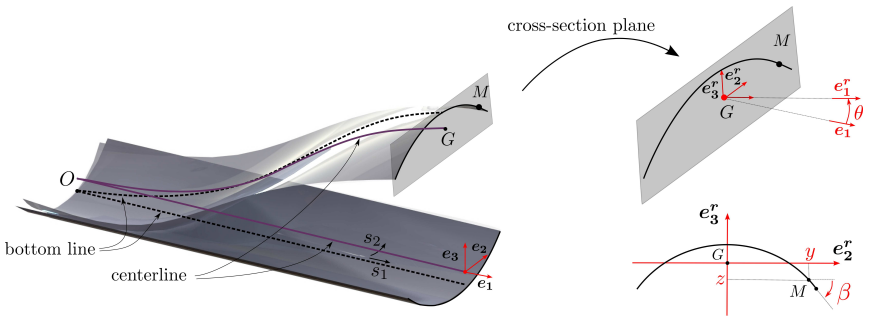

Figure 10: Kinematics of the tape spring (according to Guinot et al. (2012))

four assumptions are made :

(i) the cross-section curve remains in a plane;

(ii) the centerline remains in the plane $(O, \boldsymbol{e_1}, \boldsymbol{e_3})$ and the shell middle surface remains symmetrical with respect to this plane (planar motion);

(iii) the cross-section plane remains orthogonal to the centerline;

(iv) the cross-section curve is inextensible.

Let M be a point of the shell middle surface. Its position vector is given by

$$\boldsymbol{OM}(s_1, s_2) = \boldsymbol{OG}(s_1) + \boldsymbol{GM}(s_1, s_2) \tag{7}$$

in which G is the centroid of the cross-section that contains the point M. Let us introduce the rotated orthonormal system $(\boldsymbol{e_1^r}, \boldsymbol{e_2^r}, \boldsymbol{e_3^r})$ attached to the cross-section plane. Due to the planar motion assumption, the frame $(\boldsymbol{e_1^r}, \boldsymbol{e_2^r}, \boldsymbol{e_3^r})$ results from a rotation around the axis $\boldsymbol{e_2}$ characterized by an angle $\theta(s_1)$

and the position vectors can be expressed as :

$$\left\{ \begin{array}{lcl} \boldsymbol{OG} & = & (s_1 + u_1(s_1))\,\boldsymbol{e_1} + u_3(s_1)\,\boldsymbol{e_3}, \\ \boldsymbol{GM} & = & y(s_1, s_2)\,\boldsymbol{e_2^r} + z(s_1, s_2)\,\boldsymbol{e_3^r}(\theta(s_1)), \end{array} \right. \tag{8}$$

in which $u_1(s_1)$ and $u_3(s_1)$ are the displacements components of the centerline and (y,z) are the coordinates of point M in the rotated local frame $(G, \boldsymbol{e_2^r}, \boldsymbol{e_3^r})$. The inextensibility condition of the cross-section curve leads to the constraint: $(y_{,2})^2 + (z_{,2})^2 = 1$. The coordinates y and z can then be expressed with the angle $\beta(s_1, s_2)$ between the axis $(G, \boldsymbol{e_2^r})$ and the tangent of cross-section curve (see Figure 10) : $y_{,2} = \cos(\beta)$ and $z_{,2} = \sin(\beta)$. In the initial configuration, $\beta = s_2/R_0$. For shallow tape springs, this angle is small: $a/R_0 << 1$). We assume in the following that it remains small, leading to :

$$y(s_1, s_2) \approx s_2 \text{ and } z(s_1, s_2) \approx \int_0^{s_2} \beta(s_1, \tau)\,\mathrm{d}\tau - \frac{1}{2a}\int_{-a}^{a}\int_0^{s_2} \beta(s_1, \tau)\,\mathrm{d}\tau\,\mathrm{d}s_2. \tag{9}$$

Only four kinematic variables are needed to describe this rod model with flexible cross-section: $u_1(s_1)$, $u_3(s_1)$, $\theta(s_1)$ and $\beta(s_1, s_2)$. It must be noticed that these variables are linked by the orthogonality condition between the cross-section plane and the centerline introduced in assumption (iii) :

$$\boldsymbol{e_3^r}.\boldsymbol{OG_{,1}} = 0. \tag{10}$$

In the following, this kinematic model will be called *RFleXS-2DS* for *RFleXS* model in *2D* for *S*hallow tape springs.

3.2. Strain energy of the rod model with flexible cross-section

The material is assumed to be elastic and the kinematic assumptions are introduced in the strain energy of the shell model. We then proceed to an

integration over the cross-section to obtain the strain energy of the *RFleXS-2DS* model. Only the main ideas are recalled here: details can be found in the previous works (Guinot et al. (2012); Picault et al. (2014, 2016)). The shell strain energy is expressed with the Euler-Lagrange membrane strains $e_{\alpha\beta}$ and bending strains $k_{\alpha\beta}$, which are energetically conjugated to the membrane stresses $N_{\alpha\beta}$ and bending moment $M_{\alpha\beta}$. Large displacements are taken into account but strains are assumed to remain small. It is also assumed that the transverse tensile stress N_{22} remains small and that the shear energy $N_{12}\, e_{12}$ can be neglected. The shell strain energy can then be written as

$$U_e = \frac{1}{2}\int_0^L \int_{-a}^{a} A e_{11}^2 + D\left(k_{11}^2 + k_{22}^2 + 2\nu k_{11}k_{22} + 2(1-\nu)k_{12}^2\right) \mathrm{d}s_2 \mathrm{d}s_1, \quad (11)$$

in which shell membrane and bending strains are given by

$$\begin{cases} e_{11} &= e^r + z k^r + e^s \\ k_{11} &= -k^r + k^s_{11} \\ k_{22} &= k^s_{22}\,, \\ k_{12} &= k^s_{12}\,, \end{cases} \quad \text{with} \quad \begin{cases} e^r &= u_{1,1} + \frac{1}{2}(u_{1,1}^2 + u_{3,1}^2)\,, \\ k^r &= \theta_{,1}\,, \\ e^s &= \frac{1}{2} z_{,1}^2\,, \\ k^s_{11} &= z_{,11}\,, \\ k^s_{22} &= z_{,22} - z_{0,22}\,, \\ k^s_{12} &= z_{,12}\,, \end{cases} \quad (12)$$

and A and D are the tensile and bending stiffnesses of the shell: $A = Eh$ and $D = \frac{Eh^3}{12(1-\nu^2)}$ with h the thickness of the shell, E the Young's modulus and ν the Poisson's ratio. We recognize in e^r and k^r the tensile strain and curvature of a rod in the framework of large displacements, large rotations and small strains. The other terms e^s and $k^s_{\alpha\beta}$ refer to the deformation of the cross-sections. The tensile strain e^s takes into account non-linear effects due to the length variation of longitudinal fibbers when the cross-section deforms

non-uniformly along the tape. Bending strains $k^s_{\alpha\beta}$ characterize the local bending of the shell when the cross-section shape varies. Their expressions are similar to the ones used in the framework of small displacements but expressed in the frame attached to the cross-section: $k^s_{\alpha\beta} = z_{,\alpha\beta} - z_{0,\alpha\beta}$. Finally, an integration over the cross-section leads to the strain energy of the rod model:

$$U_e = \int_0^L \left(u_e^r + u_e^s + u_e^{rs}\right)\, \mathrm{d}s_1, \tag{13}$$

in which u_e^r, u_e^s and u_e^{rs} are the three terms that define the strain energy density $u_e(s_1)$ of the rod:

$$\left\{\begin{array}{l} u_e^r = \frac{1}{2}\left(2aA\left(e^r\right)^2 + \left(A\overline{z^2} + 2aD\right)\left(k^r\right)^2\right), \\ u_e^s = \frac{1}{2}\left(A\overline{\left(e^s\right)^2} + D\left(\overline{\left(k_{11}^s\right)^2} + \overline{\left(k_{22}^s\right)^2} + 2\nu\overline{k_{11}^s k_{22}^s} + 2(1-\nu)\overline{\left(k_{12}^s\right)^2}\right)\right), \\ u_e^{rs} = Ae^r\overline{e^s} + Ak^r\overline{ze^s} - D\,k^r\left(\overline{k_{11}^s} + \nu\overline{k_{22}^s}\right), \end{array}\right. \tag{14}$$

where the overline denotes an integration over s_2: $\overline{X}\left(s_1\right) = \int_{-a}^{a} X\left(s_1, s_2\right)\, \mathrm{d}s_2$.

At this stage, the model involves four kinematic variables: $u_1(s_1)$, $u_3(s_1)$, $\theta(s_1)$ and $\beta(s_1, s_2)$, from which the local coordinate $z(s_1, s_2)$ can be found with (9). In the following, the local coordinate $z(s_1, s_2)$ is used as the kinematic variable that describes the shape of the cross-section (instead of the angle $\beta(s_1, s_2)$).

3.3. Non-dimensionalization of the energy

The following quantities are introduced to scale the problem and quantify the key parameters that govern the strain energy:

$$\hat{s}_1 = \frac{s_1}{a},\ \hat{s}_2 = \frac{s_2}{a},\ \hat{u}_i(\hat{s}_1) = \frac{u_i(s_1)}{a},\ \hat{\theta}(\hat{s}_1) = \frac{R_0}{a}\,\theta(s_1),\ \hat{k}^r(\hat{s}_1) = R_0\,k^r(s_1),$$
$$\hat{z}(\hat{s}_1,\hat{s}_2) = \frac{R_0}{a^2}\,z(s_1,s_2) \text{ and } \hat{u}_e(\hat{s}_1) = \frac{R_0^2}{2aD}u_e(s_1). \tag{15}$$

The nondimensional expressions of the three terms (14) of the strain energy $u_e(s_1)$ can then be written as

$$\begin{cases} \hat{u}_e^r = \dfrac{1}{2}\left(12Z^2Z_\beta^4\,(\hat{e}^r)^2 + \left(6Z^2\overline{\hat{z}^2}+1\right)\left(\hat{k}^r\right)^2\right), \\ \hat{u}_e^s = \dfrac{1}{2}\left(6Z^2\overline{(\hat{e}^s)^2} + \dfrac{1}{2}\left(\overline{\left(\hat{k}_{11}^s\right)^2} + \overline{\left(\hat{k}_{22}^s\right)^2} + 2\nu\overline{\hat{k}_{11}^s\hat{k}_{22}^s} + 2(1-\nu)\overline{\left(\hat{k}_{12}^s\right)^2}\right)\right), \\ \hat{u}_e^{rs} = 6Z^2Z_\beta^2\hat{e}^r\overline{\hat{e}^s} + \hat{k}^r\left(6Z^2\overline{\hat{z}\hat{e}^s} - \dfrac{1}{2}\left(\overline{\hat{k}_{11}^s} + \nu\overline{\hat{k}_{22}^s}\right)\right), \end{cases} \tag{16}$$

in which $\hat{e}^r$, $\hat{k}^r$ $\hat{e}^s$ and $\hat{k}^s_{\alpha\beta}$ are given by the non-dimensional expression of (12) involving $\hat{u}_\alpha$, $\hat{\theta}$ and $\hat{z}$ and the spatial derivative with respect to $\hat{s}_\alpha$. The overline now denotes the integration over $\hat{s}_2$: $\overline{X}\,(\hat{s}_1) = \int_{-1}^{1} X\,(\hat{s}_1,\hat{s}_2)\ \mathrm{d}\hat{s}_2$. Two non-dimensional parameters Z and Z_β appear in (16):

$$Z = \frac{\sqrt{1-\nu^2}a^2}{hR_0} \text{ and } Z_\beta = \frac{R_0}{a}. \tag{17}$$

It should be noticed that the non-dimensional parameter Z is the Batdorf parameter, which is widely used to study the buckling of cylindrical shell panels (Batdorf, 1947).

3.4. Loading condition: the pure bending test

The static bending test in opposite sense is considered in the following: opposite moments $\pm M$ are prescribed at the end cross-sections leading to a

longitudinal curvature in opposite sense with respect to the initial transverse curvature of the cross-section curve. The end cross-sections are free to translate (null forces) and free to deform. For the sake of simplicity and due to the symmetry of the problem, the origin of the fixed frame $(O, \boldsymbol{e_1}, \boldsymbol{e_2}, \boldsymbol{e_3})$ is taken at the centroid of the cross-section located in the middle of the tape. It leads to the following boundary conditions, in which $\hat{M} = R_0 M/(2aD)$ is the non-dimensional loading parameter:

$$\begin{cases} \hat{M}(l) = -\hat{M}(-l) = \hat{M}, \\ \hat{z}(l, \hat{s}_2) \text{ and } \hat{z}(-l, \hat{s}_2) \text{ free}, \\ \hat{z}_{,1}(l, \hat{s}_2) \text{ and } \hat{z}_{,1}(-l, \hat{s}_2) \text{ free}, \\ \hat{u}_1(-l) = \hat{u}_3(-l) = \hat{u}_3(l) = 0, \end{cases} \tag{18}$$

with $l = L/(2a)$. The boundary conditions on displacements $\hat{u}_1$ and $\hat{u}_3$ fix the rigid body motion. The potential elastic energy can be written as follows:

$$\begin{aligned} \hat{P}(\hat{u}_1, \hat{u}_3, \hat{\theta}, \hat{z}, \hat{\lambda}_T) = & \int_{-l}^{l} (\hat{u}_e^r + \hat{u}_e^s + \hat{u}_e^{rs}) \, \mathrm{d}\hat{s}_1 - \ (\hat{\theta}(l) - \hat{\theta}(-l))\hat{M} \\ & + \int_{-l}^{l} \hat{\lambda}_T \left((1 + \hat{u}_{1,1}) \sin(\hat{\theta}) + \hat{u}_{3,1} \cos(\hat{\theta}) \right) \mathrm{d}\hat{s}_1, \end{aligned} \tag{19}$$

in which the orthogonality condition (10) is taken into account with the Lagrange multiplier $\hat{\lambda}_T(\hat{s}_1)$. Since the end cross-sections are free to translate, the kinematic variables $\hat{u}_1$ and $\hat{u}_3$ and the Lagrange multiplier $\hat{\lambda}_T$ can be eliminated. The differentiation of the potential energy (19) with respect to $\hat{u}_1$, $\hat{u}_3$, and $\hat{\lambda}_T$ leads to $\hat{\lambda}_T(\hat{s}_1) = 0$ and $\hat{e}^r = -\frac{1}{2Z_\beta^2}\overline{\hat{e}^s}$. The potential energy can then be rewritten:

$$\hat{P}(\hat{\theta}, \hat{z}) = \int_{-l}^{l} (\hat{u}_e^r + \hat{u}_e^s + \hat{u}_e^{rs}) \, \mathrm{d}\hat{s}_1 - \ (\hat{\theta}(l) - \hat{\theta}(-l))\hat{M} \ , \tag{20}$$

with

$$\begin{cases} \hat{u}_e^r = \dfrac{1}{2}\left(3Z^2\left(\overline{\hat{e}^s}\right)^2 + \left(6Z^2\overline{\hat{z}^2}+1\right)\left(\hat{k}^r\right)^2\right), \\ \hat{u}_e^s = \dfrac{1}{2}\left(6Z^2\overline{(\hat{e}^s)^2} + \dfrac{1}{2}\left(\overline{\left(\hat{k}_{11}^s\right)^2} + \overline{\left(\hat{k}_{22}^s\right)^2} + 2\nu\overline{\hat{k}_{11}^s\hat{k}_{22}^s} + 2(1-\nu)\overline{\left(\hat{k}_{12}^s\right)^2}\right)\right), \\ \hat{u}_e^{rs} = -3Z^2\left(\overline{\hat{e}^s}\right)^2 + \hat{k}^r\left(6Z^2\overline{\hat{z}\hat{e}^s} - \dfrac{1}{2}\left(\overline{\hat{k}_{11}^s} + \nu\overline{\hat{k}_{22}^s}\right)\right). \end{cases} \tag{21}$$

In the case of opposite sense bending test, the problem is governed by only three non-dimensional parameter: the Batdorf number Z, the Poisson's ration ν and the slenderness of the tape-spring l.

3.5. arc-of-circle flexible cross-section assumption

The parametrization proposed in (Guinot et al. (2012); Picault et al. (2014, 2016)) is here used: the cross-section shape is assumed to remain an arc-of-circle as illustrated in Figure 10. In this case, the dimensionless angle $\hat{\beta} = a\beta/R_0$ is linear with respect to $\hat{s}_2$ and takes the form $\hat{\beta}(\hat{s}_1, \hat{s}_2) = \hat{\beta}^e(\hat{s}_1)\hat{s}_2$ with $\hat{\beta}^e(\hat{s}_1) = \hat{\beta}(\hat{s}_1, 1)$. The cross-section shape is then described by $\hat{z}$ with equations (9) and (15):

$$\hat{z} = \hat{\beta}^e(\hat{s}_1)\left(\frac{\hat{s}_2^2}{2} - \frac{1}{6}\right). \tag{22}$$

This last expression is introduced in the potential energy defined by (20) and (21). The stationarity conditions with respect to $\hat{\theta}$ and $\hat{\beta}^e$ lead to the strong form of the equilibrium equations for $\hat{s}_1 \in [-l, l]$:

$$\begin{aligned} &\left(\tfrac{4}{15}Z^2\hat{\beta}^{e^2}+1\right)\hat{\theta}_{,1} + \tfrac{4}{315}Z^2\hat{\beta}^e\hat{\beta}^{e^2}_{,1} - \nu\left(\hat{\beta}^e - 1\right) = \hat{M}, \\ &\tfrac{4}{15}Z^2\hat{\beta}^e\hat{\theta}^2_{,1} - \left(\tfrac{4}{315}Z^2\left(\hat{\beta}^{e^2}_{,1} + 2\hat{\beta}^e\hat{\beta}^e_{,11}\right) + \nu\right)\hat{\theta}_{,1} - \tfrac{8}{315}Z^2\hat{\beta}^e\hat{\beta}^e_{,1}\hat{\theta}_{,11} \\ &\quad + \tfrac{1}{45}\hat{\beta}^e_{,1111} - \tfrac{2}{3}(1-\nu)\hat{\beta}^e_{,11} + \hat{\beta}^e - 1 - \tfrac{16}{1575}Z^2\hat{\beta}^{e^2}_{,1}\hat{\beta}^e_{,11} = 0, \end{aligned} \tag{23}$$

with following boundary conditions at end cross-sections $\hat{s}_1 = \pm l$ (cross-sections free to deform):

$$\begin{cases} -\frac{1}{45}\hat{\beta}^e_{,111} + \frac{2}{3}(1-\nu)\,\hat{\beta}^e_{,1} + \frac{16}{4725}\hat{\beta}^{e^2}_{,1} + \frac{8}{315}Z^2\hat{\beta}^e\hat{\beta}^e_{,1}\hat{\theta}_{,1} = 0, \\ \hat{\beta}^e_{,11} = 0. \end{cases} \tag{24}$$

4. Links with a reguralized Ericksen bar model

4.1. The fundamental solution

Starting from the initial free state $\hat{\theta}(\hat{s}_1) = 0$ and $\hat{\beta}^e(\hat{s}_1) = 1$ and $\hat{M}$ being the loading parameter of the problem, a uniform solution is found, such that the longitudinal curvature $\hat{k}^r = \hat{\theta}_{,1}$ and the cross-section shape does not depend on $\hat{s}_1$. By introducing the conditions $\hat{\theta}_{,11} = \hat{\beta}^e_{,1} = \hat{\beta}^e_{,11} = \hat{\beta}^e_{,111} = \hat{\beta}^e_{,1111} = 0$ in equations (23), closed-form expressions are obtained for the moment $\hat{M}$ and the opening angle $\hat{\beta}^e$ with respect to the uniform longitudinal curvature $\hat{k}^r$. They are denoted by $\hat{M}_u$ and $\hat{\beta}^e_u$ in the following:

$$\hat{M}_u = \hat{k}^r - \nu(\hat{\beta}^e_u - 1) + \frac{4}{15}Z^2(\hat{\beta}^e_u)^2\,\hat{k}^r \qquad \text{with} \quad \hat{\beta}^e_u = \frac{1+\nu\hat{k}^r}{1+\frac{4}{15}Z^2\hat{k}^{r2}}. \tag{25}$$

Plots of $\hat{M}_u(\hat{k}^r)$ and $\hat{\beta}^e_u(\hat{k}^r)$ are shown in Figure 11 for geometrical and material properties leading to Z=114.47 (ν=0.3). The response follows an up-down-up law and a parallel can be drawn with an Ericksen bar model. This response can be associated with a strain energy (per unit length) of a rod model defined by (21), but without the higher order terms $\hat{e}^s$, $\hat{k}^s_{11}$ and $\hat{k}^s_{12}$ (and with $\hat{\beta}^e = \hat{\beta}^e_u$).

Let us consider the response of a rod model for which the bending constitutive equation is given by (25) and shown in Figure 11 (see also Figure 20 for details). An estimate of the Maxwell moment $\hat{M}^*$ (also called *the propagating*

fold moment in literature) is obtained with the equal area rule. Assuming that $Z^2 >> 1$, considerations explained in Appendix A lead to the same estimate as the one obtained by Seffen and Pellegrino (1999): $\hat{M}^* = 1 + \nu$. Estimates are also obtained in Appendix A for the curvatures $\hat{k}_1^{r^*}$ and $\hat{k}_2^{r^*}$ which are the first and last abscissa at which the curve $\hat{M}(\hat{k}^r)$ intersects the horizontal line at ordinate $\hat{M}^*$: $\hat{k}_1^{r^*} \approx \frac{15}{4}\frac{1+\nu}{Z^2}$ and $\hat{k}_2^{r^*} \approx 1$.

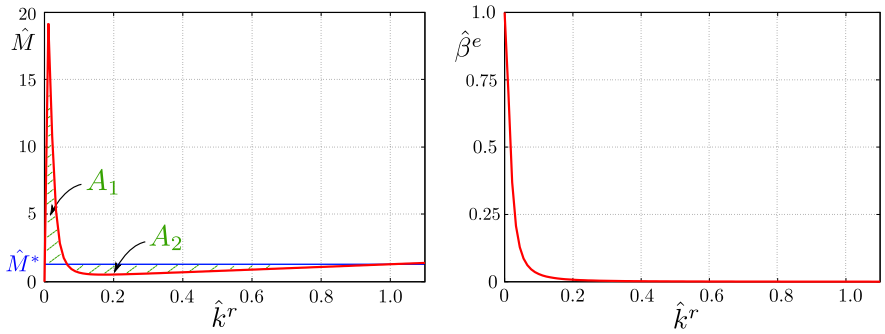

Figure 11: Bending moment $\hat{M}(\hat{k}^r)$ and opening angle $\hat{\beta}^e(\hat{k}^r)$ for $Z = 114.47$ (R_0=50 mm, a=30 mm, h=0.15 mm, E=210 000 MPa and ν=0.3) and estimate of the propagating fold moment $\hat{M}^* \approx 1 + \nu$ (Maxwell load).

Based on the results recalled in Section 2.1, Figure 12 illustrates the schematic response of the rod when rotations are applied at end cross-sections instead of a moment. The curvature $\langle \hat{k}^r \rangle$ denotes the applied average curvature: $\langle \hat{k}^r \rangle = \Delta\hat{\theta}/(2l)$ with $\Delta\hat{\theta} = \hat{\theta}(l) - \hat{\theta}(-l)$. The thick line refers to the plot of the moment $\hat{M}$ that realizes the absolute minimum of the potential strain energy for a given mean curvature $\langle \hat{k}^r \rangle$. For $\langle \hat{k}^r \rangle \leq \hat{k}_1^{r^*}$ and $\langle \hat{k}^{r^*} \rangle \geq \hat{k}_2^{r^*}$, the response follows the uniform solution. For $\hat{k}_1^{r^*} < \langle \hat{k}^{r^*} \rangle < \hat{k}_2^{r^*}$, the uniform solution is not the solution that minimizes the potential strain energy. In this regime, the moment equals the *propagating fold moment* and the deformed

shape consists in a two-phase rod with a fraction α_1 with curvature $\hat{k}_1^{r^*}$ and a fraction $\alpha_2 = 1 - \alpha_1$ with curvature $\hat{k}_2^{r^*}$, such that $\alpha_1 \hat{k}_1^{r^*} + \alpha_2 \hat{k}_2^{r^*} = \langle \hat{k}^r \rangle$, the applied average curvature. For the tape spring under consideration, the analysis of the equal area rule in Figure 11 shows that the parts with curvature $\hat{k}_1^{r^*}$ correspond to almost undeformed zones ($\hat{k}_1^{r^*} \approx 0$ and $\hat{\beta}^e(\hat{k}_1^{r^*}) \approx 1$) and parts with curvature $\hat{k}_2^{r^*}$ correspond to localized folds with flattened cross-section ($\hat{k}_2^{r^*} \approx 1$ and $\hat{\beta}^e(\hat{k}_2^{r^*}) \approx 0$). The last result shows that the fold area is cylindrical with a longitudinal curvature close to the initial transverse curvature. This property has been already mentioned by Seffen and Pellegrino (1999). Figure 12 gives an example of the deformed shape that can be obtained with two undeformed parts separated by a fold. In this figure, only one fold is introduced and this fold is arbitrary located in the middle but the model does not predict the number of phase transitions and their locations, but only the volume fraction of each phase. Jumps of curvature and of cross-section shape are allowed since no energy is associated with the variation of the cross-section shape along the tape (the higher order terms are not taken into account). The dependence of the strain energy (21) to $\hat{\beta}^e_{,1}$ and $\hat{\beta}^e_{,11}$ through the strains $\hat{e}^s$, $\hat{k}^s_{11}$ and $\hat{k}^s_{12}$ in (21) introduces in reality transition zones between the two states (see Figure 13).

4.2. Linear buckling analysis

Reintroducing the higher order terms into the strain energy and following the methodology explained in Section 2.3, a linear buckling analysis is conducted. We search for $\hat{\beta}^e$ and $\hat{\theta}$ under the forms $\hat{\beta}^e = \hat{\beta}^e_u + \Delta\hat{\beta}^e$ and $\hat{\theta} = \hat{\theta}_u + \Delta\hat{\theta}$. These forms are reported in (23) and the following first-order equations are found:

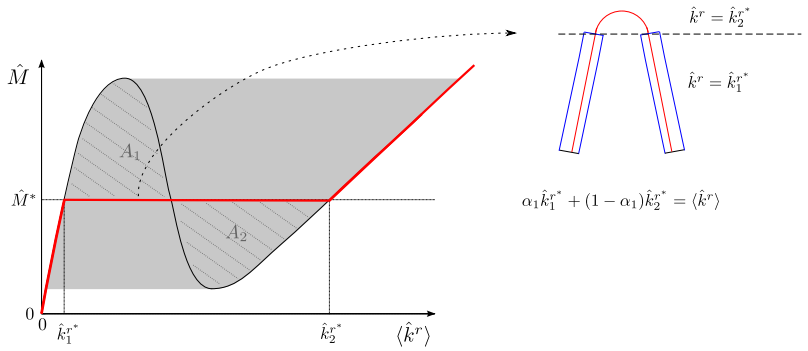

Figure 12: Plot of $\hat{M}(\langle \hat{k}^r \rangle)$ when rotations are applied at end cross-sections ($\langle \hat{k}^r \rangle = (\hat{\theta}(l) - \hat{\theta}(-l))/(2l)$). Stable solutions are reported in red line with an illustration of a two-phase rod when $\hat{k}_1^{r^*} < \langle \hat{k}^r \rangle < \hat{k}_2^{r^*}$: two almost undeformed parts located on both side of a fold with longitudinal curvature $\hat{k}_2^{r^*}$ and a flattened cross-section.

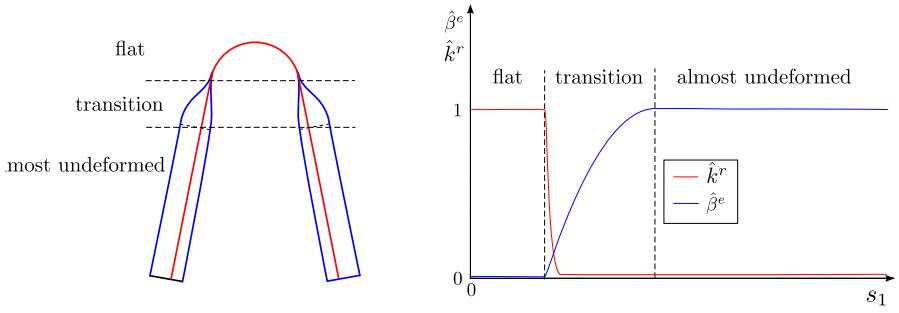

Figure 13: Illustration of the three distinct zones of deformation for a folded tape spring. Left: profile view of the deformed shape (centerline in red, exterior edge in blue). Right: evolution of the non-dimensional opening angle $\hat{\beta}^e$ and the non-dimensional longitudinal curvature $\hat{k}^r$ along the centerline in one half of the tape.

$$\begin{aligned} &\Delta\hat{\beta}^e_{,1111} - b(\hat{k}^r_u)\,\Delta\hat{\beta}^e_{,11} + c(\hat{k}^r_u)\,\Delta\hat{\beta}^e = 0, && \text{for } \hat{s}_1 \in [-l, l]\,, \\ &\Delta\hat{\beta}^e_{,111} - b(\hat{k}^r_u)\,\Delta\hat{\beta}^e_{,1} = 0, && \text{for } \hat{s}_1 = \pm l, \\ &\Delta\hat{\beta}^e_{,11} = 0, && \text{for } \hat{s}_1 = \pm l. \end{aligned} \tag{26}$$

with

$$\begin{aligned} b(\hat{k}_u^r) &= 45\left(\tfrac{8}{315}Z^2\hat{\beta}_u^e\hat{k}_u^r + \tfrac{2}{3}(1-\nu)\right), \\ c(\hat{k}_u^r) &= 45\left(1 + \tfrac{4}{15}Z^2\hat{k}_u^{r^2} - \frac{\left(\frac{8}{15}Z^2\hat{\beta}_u^e\hat{k}_u^r - \nu\right)^2}{1+\frac{4}{15}Z^2\hat{\beta}_u^{e^2}}\right). \end{aligned} \tag{27}$$

Bifurcations points are detected in the decreasing part of the plot $\hat{M}_u(\hat{k}_u^r)$, *i.e.* for $\hat{k}_u^r$ such that $\frac{\mathrm{d}\hat{M}_u}{\mathrm{d}\hat{k}_u^r} < 0$. We are then looking for roots of the characteristic polynomial $x^2 - bx + c$ associated with the ODE (26) for $\hat{k}_u^r$ in this part. It can be easily shown that $c(\hat{k}_u^r)\frac{\mathrm{d}\hat{M}_u}{\mathrm{d}\hat{k}_u^r} \geq 0$, for all $\hat{k}_u^r$. In the decreasing part of $\hat{M}_u(\hat{k}_u^r)$, c is then negative and the discriminant $b^2 - 4c$ is positive. In addition, b is positive for $\hat{k}_u^r \geq 0$ and $-1 \leq \nu \leq 0.5$. The characteristic polynomial $x^2 - bx + c$ has then two real roots of opposite signs and the general solution of the ODE in (26) for $\hat{k}_u^r$ such that $\frac{\mathrm{d}\hat{M}_u}{\mathrm{d}\hat{k}_u^r} < 0$ is:

$$\Delta\hat{\beta}^e(s_1) = D_1\cosh(r_1\,s_1) + D_2\sinh(r_1\,s_1) + D_3\cos(r_2\,s_1) + D_4\sin(r_2\,s_1)$$

with

$$r_1(\hat{k}_u^r) = \sqrt{\frac{1}{2}\left(b + \sqrt{b^2-4c}\right)} \text{ and } r_2(\hat{k}_u^r) = \sqrt{-\frac{1}{2}\left(b - \sqrt{b^2-4c}\right)},$$

and D_i some constants that must be determined with boundary conditions. Let us define the following auxiliary functions:

$$f_1(\hat{k}_u^r) = -\frac{r_2}{r_1}\frac{r_1^2-b}{r_2^2+b}\tanh(r_1 l) \quad \text{and} \quad f_2(\hat{k}_u^r) = \frac{r_1}{r_2}\frac{r_2^2+b}{r_1^2-b}\tanh(r_1 l). \tag{28}$$

The four boundary conditions in (26) lead to two sets of solutions :

(a) odd buckling mode shapes for $\hat{k}_u^r$ such that $\tan\left(r_2(\hat{k}_u^r)\,l\right) = f_1(\hat{k}_u^r)$ and

$$\Delta\hat{\beta}^e(s_1) = D_2\left(\sinh(r_1\,s_1) + d_4\sin(r_2\,s_1)\right) \text{ with } d_4 = \frac{r_1^2}{r_2^2}\frac{\sinh(r_1 l)}{\sin(r_2 l)}. \tag{29}$$

(b) even buckling mode shapes for $\hat{k}_u^r$ such that $\tan\left(r_2(\hat{k}_u^r)\, l\right) = f_2(\hat{k}_u^r)$ and

$$\Delta\hat{\beta}^e(s_1) = D_1\left(\cosh(r_1\, s_1) + d_3\cos(r_2\, s_1)\right) \text{ with } d_3 = \frac{r_1^2}{r_2^2}\frac{\cosh(r_1 l)}{\cos(r_2 l)}. \tag{30}$$

Values of $\hat{k}_u^r$ at which there is a bifurcation are then the abscissa at which the plot of $r_2(\hat{k}_u^r)l$ intersects the plots of $\arctan(f_1(\hat{k}_u^r)) + n\pi$ and $\arctan(f_2(\hat{k}_u^r)) + n\pi$, with $n \in \mathbb{N}$. An illustration is presented in Figure 14 for a short tape-spring rod (l=2.5) with a relatively small Batdorf parameter (Z=22.9). The plot of $r_2(\hat{k}_u^r)l$ is bell-shaped and the plots of $\arctan(f_1(\hat{k}_u^r)) + n\pi$ and $\arctan(f_2(\hat{k}_u^r)) + n\pi$ form a set of almost flat plateaux at values $i\pi/2$ with $i \in \mathbb{N}^+$. The situation is extremely similar to the one obtained in Section 2.3 for the classical reguralized Ericksen bar model. A finite number of bifurcation points is found. Each plateau intersects the plot of $r_2(\hat{k}_u^r)l$ in two points A_k and B_k. For a fixed k, A_k and B_k correspond to bifurcation points with the same linear buckling mode shape.

Remarks: Quantities r_1, r_2 and b only depend on Z, ν and $\hat{k}_u^r$ and are independent from l: they are independent from the slenderness of the tape. In practice, $\tanh(r_1 l)$ is very close to one and f_1 and f_2 can be considered independent from l (see equation (28)) and we obtain $f_2 \approx -1/f_1$. The two conditions $\tan(r_2\, l) = f_1$ and $\tan(r_2\, l) = f_2$ then result in a single one: $r_2\, l = \arctan(f_1) + i\pi/2$. Figure 14 illustrates this result: whatever the condition, the shape of the almost flat plateaux is the same and these plateaux are separated by a distance of $\pi/2$ in the vertical direction. Change in slenderness (*i.e.* in l) only results in a linear transformation of the plot $r_2\, l$ in the vertical direction. Increase in l leads to an increasing number of bifurcation

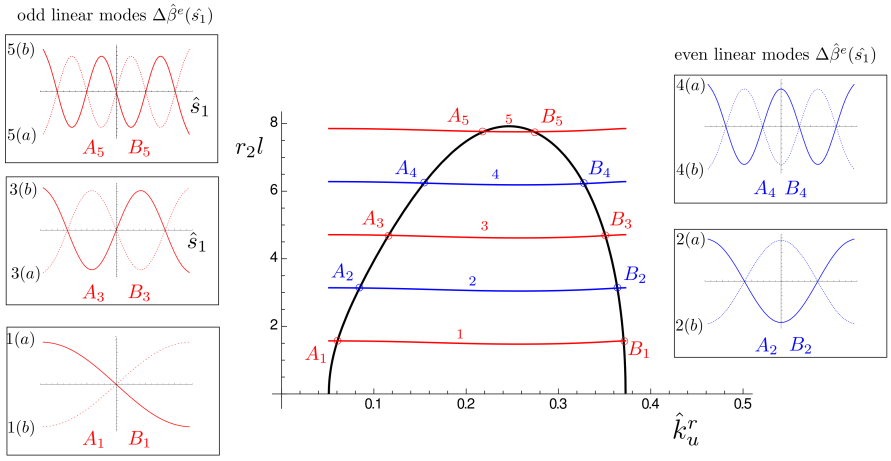

Figure 14: Graphical determination of the bifurcation points for the pure bending test in opposite sense for a tape spring with Z=22.9 and l=2.5 (L = 75mm, R_0=18.75 mm, a=15 mm, h=0.5 mm and ν=0.3). Black line: plot of $r_2(\hat{k}_u^r)l$. Red almost flat plateaux with odd index k: plots of $\arctan(\mathrm{f}_2(\hat{k}_u^r)) + (k-1)\pi/2$. Blue almost flat plateaux with even index k: plots of $\arctan(\mathrm{f}_1(\hat{k}_u^r)) + k\pi/2$. Intersection points A_k and B_k give the values of $\hat{k}_u^r$ at which there is a bifurcation. Boxes: linear buckling modes at bifurcation points A_k and B_k.

points. One can notice that the results are independent from the Young's Modulus.

4.3. Post-bifurcation analysis

A finite element implementation of the problem (23) has been performed in the software Manlab ManLab-4.0 (2018). The 1D-model is discretized with classical FE with linear Lagrange interpolation for $\hat{\theta}$ and third-order Hermite interpolation for $\hat{\beta}^e$. The bifurcation diagram obtained for the tape-spring rod with the characteristics used for Figure 14 is presented in Figure 15. The abscissas of the bifurcation points coincide with those obtained in Figure 14.

The scenario is the same as the one explained in the previous Section on the reguralized Ericksen bar model. The bifurcation points corresponding to the same linear buckling modes are connected in pairs by loops. Each loop k can be associated with post buckling shapes with k transition zones separating almost undeformed parts and flattened cross-section parts: red (resp. blue) loops for odd (resp. even) numbers of transition zones. Points A_k and B_k split each loop k in two half-loops. The two half-loops correspond to two post-buckling mode shapes with two different locations of the transition zones (see the boxes in Figure 15). In the case of odd number of transition zones (odd k), projections of the half-loops in the plane $(\langle \hat{k}^r \rangle, \hat{M})$ are superposed: the two post-buckling modes are symmetrical to one another with respect to middle cross-section and it leads to the same overall response $\hat{M}(\hat{k}^r)$. The loops corresponding to a small number of transition zones present more or less a plateau at the value of the propagating fold moment $\hat{M}^*$.

Figure 16 shows an extract of the bifurcation diagram for a tape with Z=114.7, l=19.5 and ν=0.3. In this case, the linear buckling analysis (not presented here) shows that there are 68 pairs of bifurcation points. Only the first four loops are shown in Figure 16 with the associated post-buckling shapes. Loops present more clearly a plateau at the value $\hat{M}^*$ than in figure 15 (larger Z and l). Some secondary bifurcation points are detected on the loops but they are not studied here.

4.4. Influence of the boundary conditions

All the above results have been obtained for a tape with cross-sections free to deform at ends ($\hat{\beta}^e$ and $\hat{\beta}^e_{,1}$ free at $\hat{s}_1 = \pm l$). Figure 17 compares this

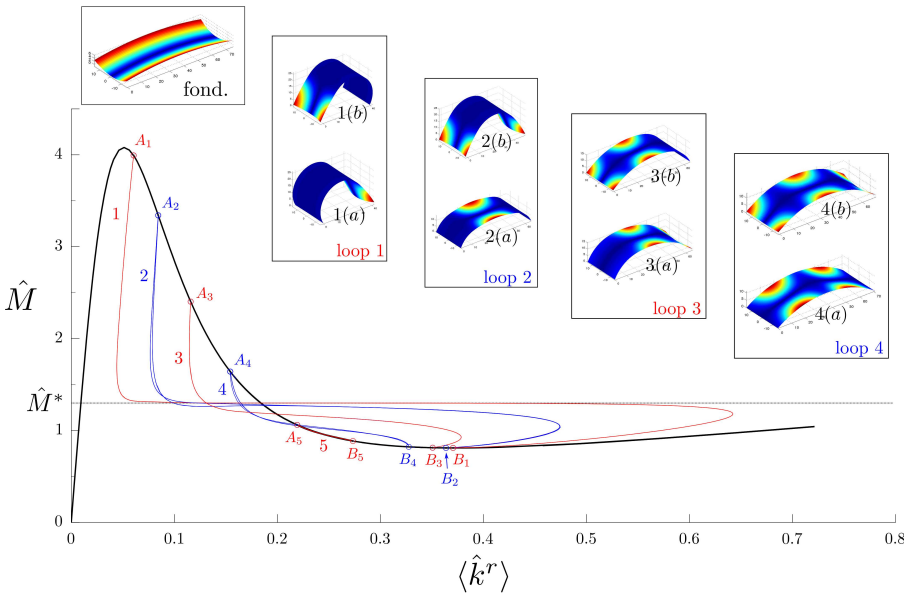

Figure 15: Bifurcation diagram for the pure bending test in opposite sense for a tape spring rod with Z=22.9 and l=2.5 (L = 75mm, R_0=18.75 mm, a=15 mm, h=0.5 mm, E=210 000 MPa and ν=0.3). Post-bifurcation branches follow a structure of loops connected to the fundamental one at two points. Each loop i corresponds to post-bifurcation modes with i transition zones separating almost undeformed parts and flattened cross-section parts. In boxes: deformed shapes observed for each half-loop defined by $A_i - B_i$. Superimposed colormap of $\hat{\beta} = \hat{\beta}^e(\hat{s}_1)\hat{s}_2$ between 0 (blue) to 1 (red).

case (bifurcation diagram in black lines) with the case of rigid cross-sections at ends (red curve): $\hat{\beta}^e = \hat{\beta}^e_0$ and $\hat{\beta}^e_{,1} = 0$ for $\hat{s}_1 = \pm l$. Fixing the cross-section shape at ends acts as a perturbation to the initial problem and there is no bifurcation point any more near the peak moment. The response is fundamentally the same as the one of a reguralized Ericksen bar model with Dirichlet boundary conditions at ends (see Figure 9). The response is very close to the fundamental branch at the beginning and turns quite smoothly

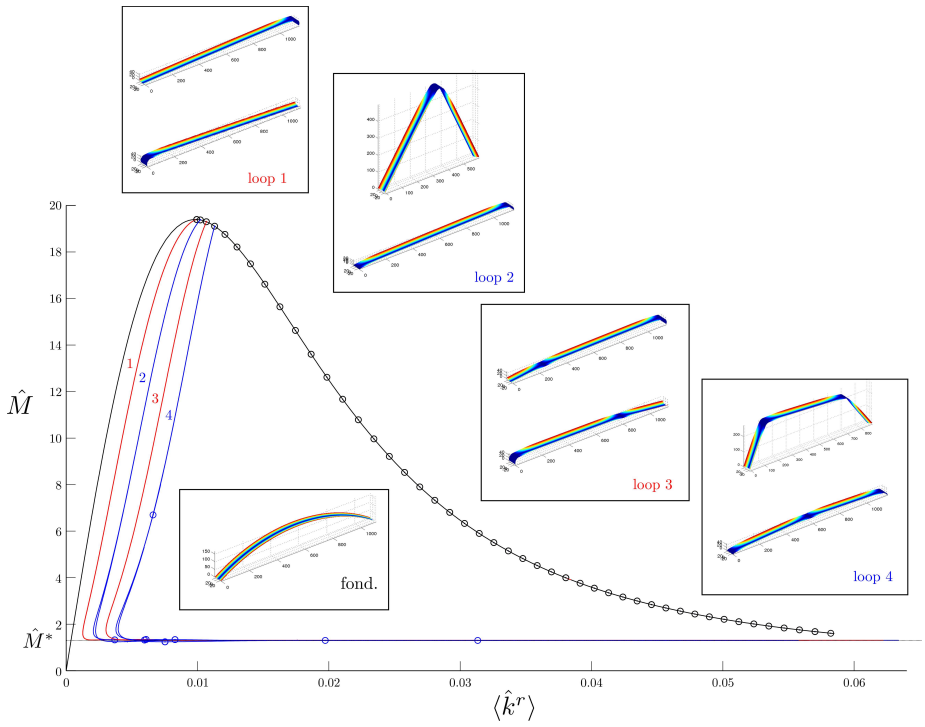

Figure 16: Bifurcation diagram for the pure bending test in opposite sense for a tape spring rod with Z=114.7 and l=19.5 (L = 1170mm, R_0=50 mm, a=30 mm, h=0.15 mm and ν=0.3). Fundamental branch and four first post-bifurcation loops. In boxes: mode shapes observed for these loops. Superimposed colormap of $\hat{\beta} = \hat{\beta}^e(\hat{s}_1)\hat{s}_2$ between 0 (blue) to 1 (red).

to follow a branch of the second loop. If we look at Figures 15 and 16, this branch corresponds to the first post-bifurcation shape 2(b) that is compatible with the new boundary conditions (undeformed cross-sections at ends) and leads to the formation and growth of a localized fold at the middle of the tape. The back return between the peak moment and the plateau explains the hysteretic behaviour that occurs for a loading-unloading prescribed average curvature (jumps of moments at limit points). The model is able to take

into account the large length effects linked to the boundary conditions and to predict the number of transition zones and their locations.

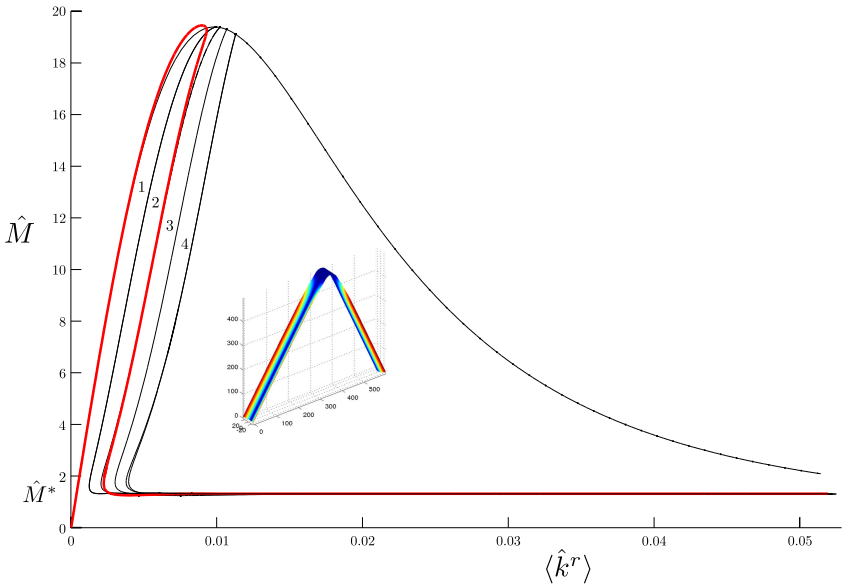

Figure 17: Bifurcation diagram for the pure bending test in opposite sense for a tape spring rod with Z=114.7 and l=19.5. Black lines: fundamental branch and first four post-bifurcation loops for end cross-sections free to deform (von-Neumann boundary conditions on higher order terms). Red curve: response with rigid end cross-sections (Dirichlet boundary conditions). In box: deformed shape observed on the plateau for rigid end cross-sections. Superimposed colormap of $\hat{\beta} = \hat{\beta}^e(\hat{s}_1)\hat{s}_2$ between 0 (blue) to 1 (red).

4.5. Lengths of the transition zones

The length of the transition zones between flattened cross-section parts and almost undeformed parts plays an important role in the maximum number of folds that can appear. In the following, a simplified approach is proposed to estimate this length. Figure 13 shows that the longitudinal curvature $\hat{k}^r$ is close to 0 in a large part of the transition zone: $\hat{k}^r$ passes from $\hat{k}_2^{r^*} \approx 1$ to $\hat{k}_1^{r^*} \approx 0$ on a much shorter distance than the one for $\hat{\beta}^e$ to pass from $\hat{\beta}^e \approx 0$ to $\hat{\beta}^e \approx 1$. Introducing $\hat{\theta}_{,1} = \hat{\theta}_{,11} = 0$ in the second equation of (23) leads to:

$$\frac{1}{45}\hat{\beta}^e_{,1111} - \frac{2}{3}(1-\nu)\,\hat{\beta}^e_{,11} + \hat{\beta}^e - 1 - \frac{16}{1575}Z^2\hat{\beta}^{e^2}_{,1}\,\hat{\beta}^e_{,11} = 0. \tag{31}$$

Figure 18 shows that the length of the transition zone increases with Z

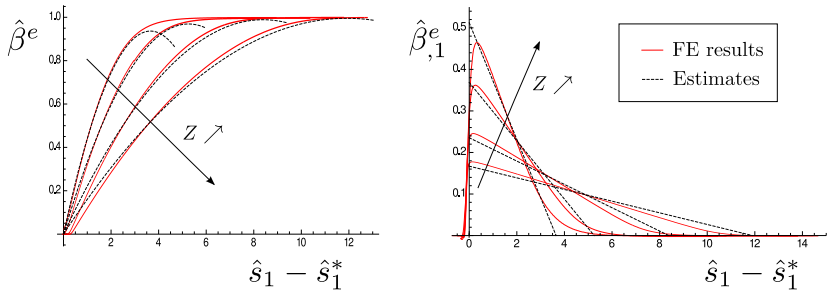

Figure 18: Evolution of $\hat{\beta}^e$ and $\hat{\beta}^e_{,1}$ (cross-section shape) in the transition zone for several values of the Batdorf parameter: $Z = 50,\ 100,\ 250, 500$ (and $l > 20$). Red lines: FE results obtained with the proposed rod model. Black dashed lines: estimates.

and that $\hat{\beta}^e_{,1}$ is almost affine in a large central part (FE results obtained with the *RFleXS-2DS* model in red). Neglecting the localized effects at the beginning of the transition zone (rapid changes in $\hat{\beta}^e_{,1}$), the estimate $\hat{\beta}^e = c_1\,(\hat{s}_1 - \hat{s}_1^*) - \frac{1}{2}c_2\,(\hat{s}_1 - \hat{s}_1^*)^2$ is introduced in equation (31), with $\hat{s}_1^*$ the

starting abscissa of the transition zone. A power series in $(\hat{s}_1 - \hat{s}_1^*)$ is obtained and constants c_1 and c_2 are identified by vanishing the first two terms:

$$c_1 = \sqrt{\frac{525}{8}\frac{1}{Z^2}\left[\frac{2}{5}\sqrt{\frac{2}{7}}Z - (1-\nu)\right]} \text{ and } c_2 = \frac{15}{4}\sqrt{\frac{7}{2}}\frac{1}{Z}. \tag{32}$$

Figure 18 shows good agreements between the estimates (black dashed curves) and the FE results obtained with the *RFleXS-2DS* model (red curves). For a fixed Z, the constant c_1 is the intercept of the black dashed straight line in the plot of $\hat{\beta}^e_{,1}$ and c_2 is the opposite of its slope. Length estimate of the transition zone is defined as c_1/c_2, *i.e.* the abscissa at which the black dashed straight lines intersect the x-axis in the plot of $\hat{\beta}^e_{,1}$. In practice, the term $1-\nu$ can be neglected in the expression of c_1 and the non dimensional length of the transition zone $\hat{l}_t = l_t/a$ is found to be proportional to $\sqrt{Z}$:

$$\hat{l}_t = \sqrt{\frac{8}{15}\sqrt{\frac{2}{7}}\sqrt{Z}}. \tag{33}$$

The model predicts that the non-dimensional length $\hat{l}_t = l_t/a$ mainly depends on the Batdorf parameter Z. In the following, this estimate is compared to FE shell results obtained with Abaqus. In the transition zones, the cross-section passes from flattened to undeformed. The results are compared through the evolution along the tape of the apparent (non-dimensional) total thickness, defined as $\Delta\hat{z} = \hat{z}(\hat{s}_1, \hat{s}_2 = 1) - \hat{z}(\hat{s}_1, \hat{s}_2 = 0)$. Its initial value is $\Delta\hat{z}_0$. For the shell model, the value of Δz can be easily obtained:

$$\Delta z = \sqrt{\left(\Delta u_1^s\right)^2 + \left(\Delta z_0 + \Delta u_3^s\right)^2},$$

with $\Delta u_i^s = u_i^s(s_1, s_2 = a) - u_i^s(s_1, s_2 = 0)$ and $u_i^s(s_1, s_2)$ the displacements

of the shell middle surface. When $\Delta z/\Delta z_0 = \Delta\hat{z}/\Delta\hat{z}_0$ equals one, the cross-section is undeformed and a value of zero corresponds to a flattened cross-section. Numerical simulations have been performed with FE shell models in opposite sense bending with rigid cross-sections at ends, for several values of the geometric parameters and of the Poisson ratio, leading to a range of the Batdorf parameter Z from 50 to 500 (see Table 2). This loading leads to the creation of a localized fold in the middle of the tape. Figure 19 shows the evolution of $\Delta\hat{z}/\Delta\hat{z}_0$ with respect to $\hat{s}_1 = s_1/a$ for varying values of the parameters a, R_0, h and ν. The origin of the abscissa $\hat{s}_1$ has been adapted for each plot so that the transition zone begins at the same abscissa. The plots corresponding to the same value of the Batdorf parameter Z are very close together. This parameter seems to be the key parameter that governs the length of the transition zones. The comparison between the FE shell and the FE *RFleXS-2DS* results exhibits some discrepancies, especially for large Z. Nevertheless, the two models lead to quite the same estimates of the lengths of the transition zones for all Z. The expression (33) can then constitute a satisfactory estimate for the lengths of the transition zone.

5. Comparison with shell models

5.1. Introduction

The behaviour of tape springs is often studied with shell models. This section addresses the validation of the overall response $\hat{M}(\hat{k}^r)$ obtained with the *RFleXS-2DS* model and the ones obtained with reference shell models.

case	a (mm)	R_0 (mm)	h (mm)	ν	Z
(a)	13.1036	21.8393	0.15	0.3	50
(b)	26.2071	87.3571	0.15	0.3	50
(c)	26.2071	43.6785	0.3	0.3	50
(d)	26.2071	43.6785	0.3145	0	50
(e)	26.2071	43.6785	0.2749	0.49	50
(f)	26.2071	43.6785	0.15	0.3	100
(g)	65.5178	109.1963	0.15	0.3	250
(h)	131.0356	218.3927	0.15	0.3	500
(j)	262.0712	873.5707	0.15	0.3	500
(j)	524.1424	1747.1414	0.3	0.3	500

Table 2: Geometric and material parameters used for the parametric study of the lengths of the transition zones

5.2. The model of Wuest

Closed form estimate of the overall response $\hat{M}(\hat{k}^r)$ has been obtained by Wuest (1954) for the fondamental solution (uniform longitudinal curvature and loading-dependent uniform cross-section profile along the tape). This estimate is based on the assumption that the tape spring can be assimilated as a slightly distorded axisymmetric shell submitted to pure bending. In the *RFleXS-2DS* model, the cross-section is assumed to remain an arc-of-circle cross-section. When searching for a uniform solution, this assumption can be removed and it is shown in this case that the Wuest estimate is found .

The end cross-sections are assumed to be free to deform. Starting from the potential elastic energy defined by (20), (21) and the non-dimensional

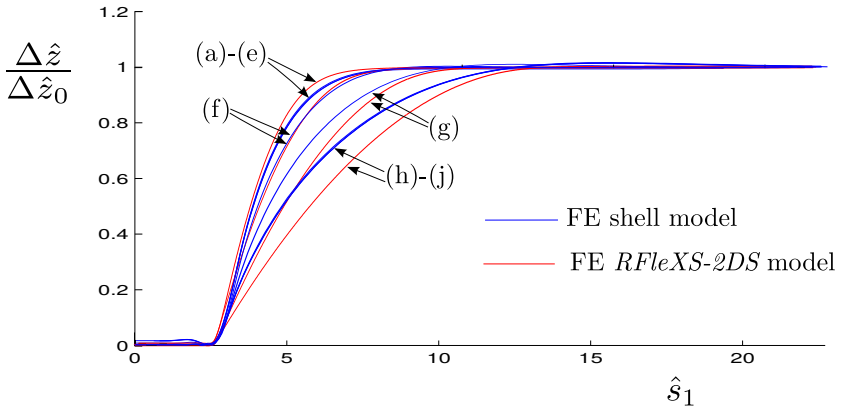

Figure 19: Evolution of the apparent total thickness of the tape in the transition zone between the fold and the almost undeformed area. Comparison between the *RFleXS-2DS* and the shell models for several values of the geometric and material properties corresponding to the cases (a)-(j) reported in Table 2.

expressions of (12), a uniform solution is searched such that the longitudinal curvature $\hat{k}^r = \hat{\theta}_{,1}$ is constant and the kinematic variable $\hat{z}$ only depends on $\hat{s}_2$. Taking into account these properties, the potential energy can be written as

$$\hat{P}(\hat{k}^r, \hat{z}) = 2l \int_{-1}^{1} \left[\left(6Z^2\hat{z}^2 + 1\right) \hat{k}^{r^2} + \frac{1}{4} \left(\hat{z}_{,22} - 1\right)^2 - \frac{\nu}{2} \left(\hat{z}_{,22} - 1\right) \hat{k}^r \right] \mathrm{d}\hat{s}_2 - 2l\hat{M}\hat{k}^r. \tag{34}$$

The stationarity condition of the potential energy leads to the differential equation that governs the cross-section shape:

$$\hat{z}_{,2222} + 12Z^2 k^{r^2} \hat{z} = 0, \quad \text{for } \hat{s}_2 \in [-1, 1], \tag{35}$$

with

$$\begin{cases} (\hat{z}_{,22} - 1) - \nu\hat{k}^r = 0, & \text{for } \hat{s}_2 = \pm 1, \\ \hat{z}_{,222} = 0, & \text{for } s_2 = \pm 1, \end{cases} \tag{36}$$

These last equations (36) correspond to free edge conditions (shell bending moment $\hat{m}_{22}$ and shear force $\hat{t}_2$ are vanishing for $\hat{s}_2 = \pm 1$). The solution of equations (35) and (36) provides the cross-section profile with respect to the longitudinal curvature $\hat{k}^r$:

$$\hat{z} = \alpha_1 \cosh(n\hat{s}_2\hat{k}^r)\cos(n\hat{s}_2\hat{k}^r) + \alpha_2 \sinh(n\hat{s}_2\hat{k}^r)\sin(n\hat{s}_2\hat{k}^r), \tag{37}$$

with $n = \sqrt[4]{3Z^2/\hat{k}^{r\,2}}$ and

$$\begin{cases} \alpha_1 = -\dfrac{1+\nu\hat{k}^r}{2n^2\hat{k}^{r\,2}} \dfrac{\cosh(n\hat{k}^r)\sin(n\hat{k}^r) - \sinh(n\hat{k}^r)\cos(n\hat{k}^r)}{\cosh(n\hat{k}^r)\sinh(n\hat{k}^r) + \cos(n\hat{k}^r)\sin(n\hat{k}^r)}, \\ \alpha_2 = \dfrac{1+\nu\hat{k}^r}{2n^2\hat{k}^{r\,2}} \dfrac{\cosh(n\hat{k}^r)\sin(n\hat{k}^r) + \sinh(n\hat{k}^r)\cos(n\hat{k}^r)}{\cosh(n\hat{k}^r)\sinh(n\hat{k}^r) + \cos(n\hat{k}^r)\sin(n\hat{k}^r)}. \end{cases} \tag{38}$$

The relationship between the bending moment $\hat{M}$ and the longitudinal curvature $\hat{k}^r$ is obtained by differentiation of the potential energy with respect to the longitudinal curvature $\hat{k}^r$:

$$\hat{M} = 6Z^2 \int_{-1}^{1} \hat{z}^2 \mathrm{d}s_2 \; \hat{k}^r + \int_{-1}^{1} \frac{1}{2}\left[\hat{k}^r - \nu\left(\hat{z}_{,22} - 1\right)\right] \mathrm{d}s_2. \tag{39}$$

The first term involves the second moment of area $\int_{-1}^{1} \hat{z}^2 \mathrm{d}s_2$ and is the contribution of the membrane stress $\hat{n}_{11}$. The second one is the contribution of the shell bending moment $\hat{m}_{11}$. Finally, introducing expressions (37)-(38) of $\hat{z}$ in (39) leads to the moment called $\hat{M}^W$ in the following:

$$\hat{M}^W = \hat{k}^r + \nu\left(1 + 2\left(1+\nu\hat{k}^r\right)\frac{\cos(2n\hat{k}^r)-\cosh(2n\hat{k}^r)}{2n\hat{k}^r\left(\sin(2n\hat{k}^r)+\sinh(2n\hat{k}^r)\right)}\right)$$

$$+\frac{1}{8}\frac{\left(1+\nu\hat{k}^r\right)^2}{2n\hat{k}^{r2}}\frac{2\cosh(2n\hat{k}^r)\sin(2n\hat{k}^r)-2\left(\cos(2n\hat{k}^r)+4n\hat{k}^r\sin(2n\hat{k}^r)\right)\sinh(2n\hat{k}^r)}{\left(\sin(2n\hat{k}^r)+\sinh(2n\hat{k}^r)\right)^2} \quad (40)$$

$$+\frac{1}{8}\frac{\left(1+\nu\hat{k}^r\right)^2}{2n\hat{k}^{r2}}\frac{\sinh(4n\hat{k}^r)-\sin(4n\hat{k}^r)}{\left(\sin(2n\hat{k}^r)+\sinh(2n\hat{k}^r)\right)^2}.$$

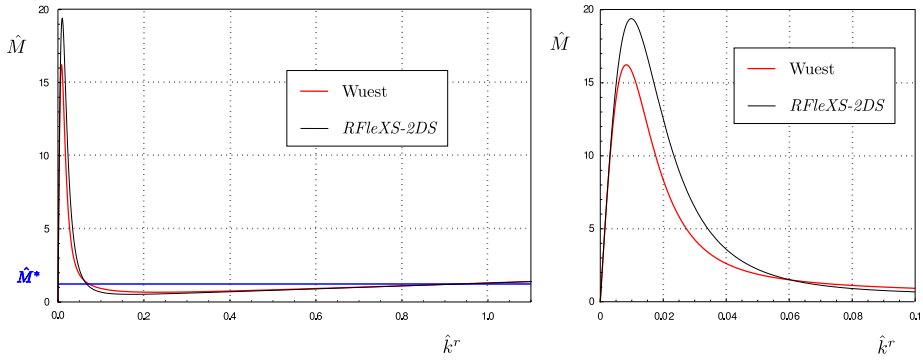

Figure 20: Bending moment $\hat{M}_u(\hat{k}^r)$ for $Z = 114.47$ (R_0=50 mm, a=30 mm, h=0.15 mm, E=210 000 MPa and ν=0.3) and propagating fold moment $\hat{M}^*$ (Maxwell load).

Equations (35)-(40) are strictly equivalent to the ones obtained by Wuest (1954) with a different approach. The Wuest estimate $\hat{M}^W(\hat{k}^r)$ is compared to the one obtained with the *RFleXS-2DS* model with an arc-of-circle cross-section in Figure 20 for Z=114.47 and ν=0.3. The two curves present a similar up-down-up response. They have the same slope in the linear part for small $\hat{k}^r$ and tend to the same asymptote $\nu + \hat{k}^r$ when $\hat{k}^r$ becomes large.

Table 3 compares some key features: the propagating fold moment $\hat{M}^*$, the longitudinal curvature in the fold area and the peak moment. Values of

	$\hat{M}^*$	$\hat{k}_2^{r^*}$	Peak Moment
RFleXS-2DS	1.30000	0.999628	19.3954
Wuest	1.23809	0.934083	16.2317

Table 3: Non-dimensional propagating fold moment $\hat{M}^*$, longitudinal curvature $\hat{k}_2^{r^*}$ and peak moment, for the *RFleXS-2DS* model and the solution of Wuest ($\nu = 0.3$ and $Z = 114.47$).

the propagating fold moment and the longitudinal curvature $\hat{k}_2^{r^*}$, which are obtained by solving Equation (A.6), are in agreement but the assumption of an arc-of-circle cross-section profile leads to an overestimate of the peak moment (19.3954 and 16.2317 for the *RFleXS-2DS* model and the Wuest estimate respectively). An enriched model is proposed in Section 5.4 to cope with this problem.

5.3. Comparison with FE shell models

Figure 21 shows typical results on the overall response in opposite sense bending with rigid end cross-sections. The FE shell results, which are taken as reference, have been obtained with the software Abaqus, using a Riks procedure and S8R5 elements (120 elements in the length direction and 12 in the transverse one). In the linear part for small $\langle \hat{k}^r \rangle$, all models are in agreement. The estimate $\hat{M}^* = 1 + \nu$ of Seffen and Pellegrino (1999) for the propagating fold moment coincides with the results of the FE shell and *RFleXS-2DS* models. We observe that the *RFleXS-2DS* model overestimates the peak moment. One can also notice that the Wuest formula for the uniform solution gives a good estimate of the peak moment. The Wuest estimate is better in accordance with the FE shell results in the beginning than the

RFleXS-2DS results. The difference between the Wuest estimate and the uniform solution found with the *RFleXS-2DS* is the cross-section kinematics: the assumption of an arc-of-circle cross-section leads to a stiff approximation. In Section 5.4, it is shown that an enrichment of the cross-section kinematics of the *RFleXS-2DS* model greatly improves the result on the peak moment.

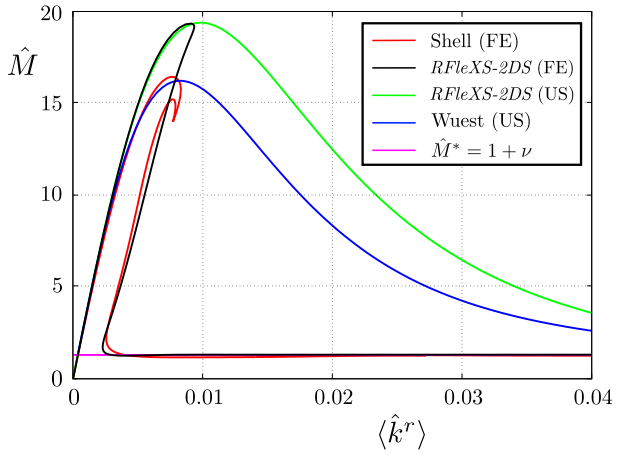

Figure 21: Dimensionless bending moment $\hat{M}$ with respect to the mean dimensionless longitudinal curvature $\langle \hat{k}^r \rangle$ obtained with several models for the pure bending test in opposite sense with rigid cross-section at ends (Z = 114.47, L=1170 mm, R_0=50 mm, a=30 mm, h=0.15 mm, E=210 000 MPa and ν=0.3). Shell model (FE): Finite Element Analysis; Wuest (US): closed-form estimate of Wuest (1954) for the uniform solution; *RFleXS-2DS* (FE): Finite Element Analysis with the *RFleXS-2DS* Model; *RFleXS-2DS* (US): closed-form expression obtained with the *RFleXS-2DS* model for the uniform solution, Estimate of the dimensionless propagating fold moment $\hat{M}^*$.

5.4. Enrichment of the cross-section kinematics

It follows from the discussion above that it is necessary to enrich the cross-section kinematics in order to obtain a good estimate of the peak moment. Let us consider the uniform solution for the opposite sense bending test without introducing the circularity assumption of the cross-section. In the expression (34) of the elastic potential energy, the term $\hat{z}_{,22}$ is the transverse curvature $\hat{\kappa}(\hat{s}_1, \hat{s}_2)$ which has been taken uniform in the *RFleXS-2DS* model since the cross-section is assumed to remain an arc-of-circle. In order to enrich this kinematics, we introduce an expansion of this transverse curvature based on the first Legendre polynomials $\hat{P}^i(\hat{s}_2)$ of order i, defined in $[-1, 1]$:

$$\hat{\kappa}(\hat{s}_1, \hat{s}_2) = \sum_{i=0}^{n} \hat{\kappa}(\hat{s}_1)\hat{P}^i(\hat{s}_2). \tag{41}$$

The components of the initial curvature in the truncated basis are denoted $\hat{\kappa}_0^i$. For a tape spring with an initially arc-of-circle cross-section, we obtain $\hat{\kappa}_0^0 = 1$ and $\hat{\kappa}_0^i = 0$ for $i > 0$. Due to the symmetry assumption of the cross-section shape, only the even polynomials are considered ($i = 2k$, $k \in \mathbb{N}^+$). The orthogonality of the Legendre polynomials leads to the following properties (valid for any initial cross-section shape):

$$\overline{(\hat{\kappa}^2)} = \hat{\kappa}^{i^2}\ \overline{(\hat{P}^i)^2} \text{ and } \overline{\hat{\kappa}} = 2a\hat{\kappa}^0.$$

We denote by $\hat{Q}^i(\hat{s}_2)$ the integral of $\hat{P}^i(\hat{s}_2)$ verifying $\hat{Q}^i(0) = 0$. According to the inextensibility assumption of the cross-section, the angle $\hat{\beta}(\hat{s}_1, \hat{s}_2)$ is expressed by:

$$\hat{\beta}(\hat{s}_1, \hat{s}_2) = \hat{\kappa}(\hat{s}_1)\hat{Q}^i(\hat{s}_2). \tag{42}$$

This last expression is still valid for non moderate angles $\beta(s_1, s_2)$ but the determination of $z(s_1, s_2)$ requires the integration of $z_{,2} = \sin(\beta)$ in this case.

In case of small angles, $z_{,2} \approx \beta$ and the polynomials $\hat{R}^i(\hat{s}_2)$, which are the integrals of $\hat{Q}^i(\hat{s}_2)$ verifying $\overline{\hat{R}^i} = 0$ can be used to obtain an expansion of $\hat{z}(\hat{s}_1, \hat{s}_2)$:

$$\hat{z}(\hat{s}_1, \hat{s}_2) = \hat{\kappa}^i(\hat{s}_1)\hat{R}^i(\hat{s}_2). \tag{43}$$

The condition $\overline{\hat{R}^i} = 0$ ensures that $\overline{\hat{z}} = 0$ (centroid property). Introducing expression (43) in the elastic potential energy (34) leads to:

$$\begin{aligned}\hat{P} = \frac{l}{2}\Bigg[\left(6Z^2\overline{\hat{R}^i\,\hat{R}^j}\,\hat{\kappa}^i\,\hat{\kappa}^j + 1\right)\left(\hat{k}^r\right)^2 + \frac{1}{2}\overline{(\hat{P}^i)^2}\,(\hat{\kappa}^i - \delta_{i0})^2 \\ -2\nu\hat{k}^r(\hat{\kappa}^0 - 1)\Bigg] - \hat{M}\hat{k}^r l,\end{aligned} \tag{44}$$

and from the stationarity conditions follows the system:

$$\left(6Z^2\overline{\hat{R}^i\,\hat{R}^j}\,\hat{\kappa}^i\,\hat{\kappa}^j + 1\right)\hat{k}^r - \nu(\hat{\kappa}^0 - 1) = \hat{M}, \tag{45}$$

$$6Z^2\overline{\hat{R}^0\,\hat{R}^j}\,\left(\hat{k}^r\right)^2\hat{\kappa}^j + \frac{1}{2}\overline{(\hat{P}^0)^2}\,\left(\hat{\kappa}^0 - 1\right) = \nu\hat{k}^r, \tag{46}$$

$$6Z^2\overline{\hat{R}^i\,\hat{R}^j}\,\left(\hat{k}^r\right)^2\hat{\kappa}^j + \frac{1}{2}\overline{(\hat{P}^i)^2}\,\hat{\kappa}^i = 0, \qquad \text{for } i = 1, ..., n. \tag{47}$$

Equations (46) and (47) form a linear system of order $n+1$ that gives the expressions of $\hat{\kappa}^i(\hat{k}^r)$. The bending response $\hat{M}(\hat{k}^r)$ is then obtained by introducing these expressions in Equation (45). Results are plotted in Figures 22 and 23 for several order of enrichment n=0, 2, 4, 6 et 8 and $Z = 114.47$ ($R_0 = 0.05$ m, a =0.03 m, h=0.00015 m, E=210000 MPa and $\nu = 0.3$). They are compared to the Wuest estimate. It is recalled that a model of order n only involves $\frac{n}{2} + 1$ degrees of freedom to describe the cross-section shape (Legendre polynomials of odd order are not introduced).

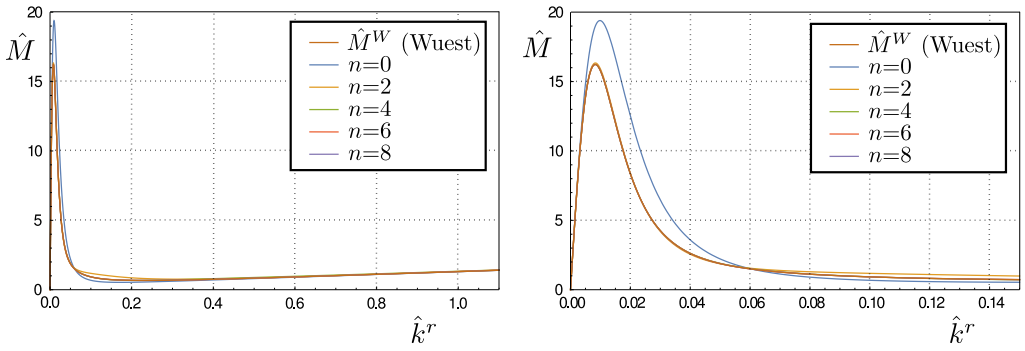

Figure 22: Bending moment $\hat{M}$ with respect to the longitudinal curvature $\hat{k}^r$ (uniform solution) for several order of enrichment and comparison with the exact solution of Wuest.

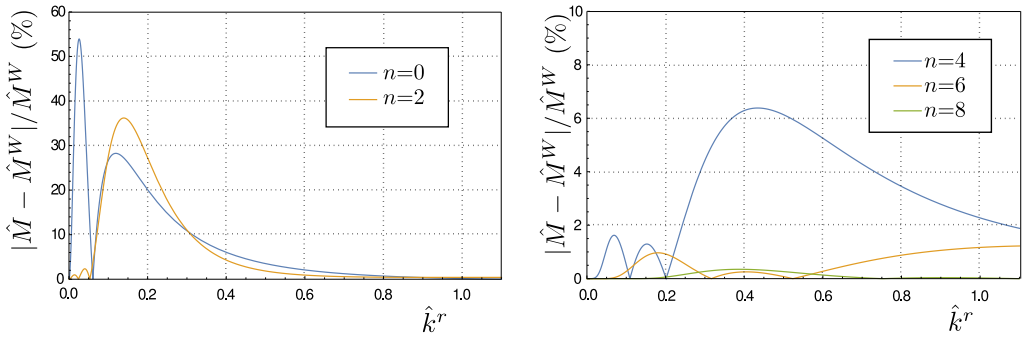

Figure 23: Relative difference (%) on $\hat{M}(\hat{k}^r)$ between the enriched model and the exact solution of Wuest for several order of enrichment.

Whatever the order of enrichment, the model has a correct asymptotic behaviour for relatively high values of the longitudinal curvature $\hat{k}^r$ (shell-dominated behaviour). Model of order 0 is strictly the same as the original model involving the only parameter β^e to describe the cross-section shape (uniform transverse curvature along the cross-section). As shown before, this model overestimates the peak moment (around 20 %). The introduction of a second degree of freedom (n=2) greatly improves its estimate but this model shows discrepancies with the analytical solution of Wuest in the tran-

	n=0	n=2	n=4	n=6	n=8	Wuest
Peak Moment	19.3954	16.3388	16.2317	16.2317	16.2317	16.2317
$\hat{M}^*$	1.30000	1.29518	1.26979	1.24191	1.23896	1.23809
$\hat{k}_2^{r^*}$	0.999628	0.987448	0.963640	0.924214	0.935430	0.934083

Table 4: non-dimensional peak moment, propagating fold moment $\hat{M}^*$ and longitudinal curvature $\hat{k}_2^{r^*}$ for several order of enrichment and the analytical solution of Wuest ($\nu = 0.3$ and $Z = 114.47$)

sition zone between the rod-dominated behaviour and the shell-dominated behaviour (see Figure 23). Models with 3, 4 and 5 dofs (n =4,6 and 7) lead to relative differences of less than 7%, 2% and 1% respectively for $0 < \hat{k}^r < 1.1$.

Some key features are reported in Table 4. These values are obtained numerically for Z=114.473 and ν=0.3. Values of $\hat{M}^*$ and $\hat{k}_2^{r^*}$ are obtained by solving Equation (A.6). Estimates of Seffen and Pellegrino (1999) are found for $n = 0$: $\hat{M}^* \approx 1 + \nu$ and $\hat{k}_2^{r^*} \approx 1$. For n =2, the peak moment is much better in accordance with the exact solution of Wuest but the propagating fold moment is not greatly improved. Very good results are obtained for n =6 and $n = 8$. The case $n = 4$ offers a good compromise between the precision and the number of dofs for the cross-section shape.

Figure 24 compares the results obtained for the opposite sense bending test with rigid end cross-sections between the *RFleXS-2DS* model for two order of enrichment and the shell model. The proposed enrichment greatly improves the initial model when compared to a shell model. The peak moment, which is overestimated with the initial model $n = 0$, is in agreement

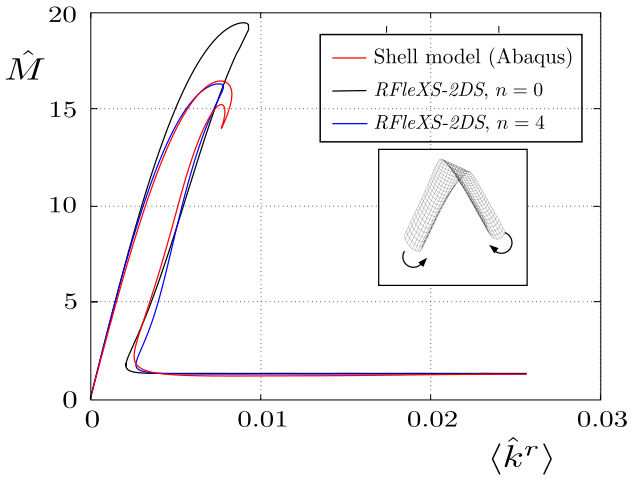

Figure 24: Opposite sense bending test with rigid cross-sections at ends. Overall response of the *RFleXS-2DS* models for two orders of enrichment compared to FE shell model.

with the shell model for the enriched model corresponding to $n = 4$. Nevertheless, the cusp observed during the back return for the shell model is not observed with the *RFleXS-2DS* models. Some investigations (not presented here) with the FE shell model have shown that the prescribed rotation (or moment) at which the cusp occurs strongly depends on the mesh refinement. The more the mesh is refined, the more the second local maximum after the cusp is close to the first one located before the cusp and it is difficult to determine the limit. Some further works are necessary to understand the origin of this back return and to determine the equilibrium branches of the continuous problem in this area.

6. Conclusion

In this work, bifurcation diagrams of a reguralized Ericksen bar model is deeply studied. A first result resides in the fact that these diagrams strongly depend on the boundary conditions prescribed on higher order terms. With von-Neumann boundary conditions, the bifurcation diagram exhibits a structure of loops that cross the fundamental branch (homogeneous solution) at two points. The number of loops is bounded and each loop corresponds to a post bifurcation shape with a given number of transition zones between extrema of strains. Considering the overall response (stress vs average strain), when the reguralized parameter is small, the loops exhibit a plateau at the Maxwell stress and the post-bifurcation shape corresponds to regions of homogeneous strains separated by small transition zones that move along the bar. Dirichlet boundary conditions acts as a perturbation to the problem with von-Neumann conditions. There are no more bifurcation points and the post-bifurcation shape is a two-phase bar with two transition zones, leading to a localization of strain in the middle of the bar.

An obvious parallel is then made with the behaviour of tape-springs. To this end, a reduced 1D rod model with an arc-of-circle flexible cross-section dedicated to the pure opposite-sense bending test of shallow tape-springs is proposed. This model involves only two kinematic variables linked to the bending rotation and the transverse curvature of the cross-sections. The analytical expression of the strain energy is found to be similar to the one of a reguralized Ericksen bar model, with the higher order terms linked to the variation of the cross-section shape along the tape. The model exhibits the same properties as the reguralized Ericsen bar: sensitivity to boundary con-

ditions on higher order terms, structure of loops for the bifurcation diagrams, localization of curvature (folds). Strong form expressions of the governing equations are obtained. It allows to propose estimates for the length of transition zones that are satisfactory compared with FE results. Analytical results are also found for the geometrical properties of the fold areas and the Maxwel moment (or *propagating fold moment*) which are in agreement with the estimates of Seffen and Pellegrino (1999).

Eventually, the overall response (bending moment vs average curvature) obtained with the rod model with flexible cross-section is compared with the ones obtained with some shell models. Considering the model of Wuest (1954) who proposed an analytical expression for the fundamental solution, discrepancies are found on the peak moment of the up-down-up constitutive law. It is shown that this analytical expression can be found with the proposed rod model when the circularity assumption of the cross-section shape is removed. An enrichment of the cross-section kinematics is then proposed and the results show good agreements with shell FE results.

In this work, it was shown that the tape-spring can be considered as a reguralized Ericksen bar. This parallel explains the mechanical behaviour of tape-spring in a deep way. It allows to confirm and complement the estimates of the mechanical key features found by Seffen and Pellegrino (1999). The reduced 1D rod model with an arc-of-circle flexible cross-section provides good estimates of the propagating fold moment and the geometric properties of locally-homogeneous parts: longitudinal and transverse curvatures in the folds and in the almost undeformed parts. These estimates do not require the reguralization terms (higher order terms) and are based on the analysis of

the purely homogeneous solution and the equal-area rule of Maxwell. Reintroducing the higher order terms, the model allows to obtain satisfactory estimates of the length of the transitions zones between the folds and the almost undeformed parts, even if the kinematics assumptions (arc-of-circle cross-section) do not capture the precise shape of the cross-section in these areas. It is also shown that the enrichment of the cross-section kinematics leads to a much better estimate of the peak bending moment during a folding test (compared to results obtained with FE shell models). Furthermore, it predicts correctly the creation of a single fold in the middle of the tape with rigid end cross-sections, when suitable boundary conditions are considered on higher order terms. More examples of quantitative comparisons with experimental results and other numerical results can be found in Picault et al. (2014): dynamics deployment of a tape spring involving a travelling fold for instance.

This approach could be a good starting point to study the number of stable folded configurations for a given loading at ends.

Acknowledgements

The work presented in this paper was supported by a doctoral grant from ANRT and Thales Alenia Space.

References

Audoly, B., Hutchinson, J. W., 2016. Analysis of necking based on a one-dimensional model. Journal of the Mechanics and Physics of Solids 97, 68–91.

Batdorf, S., 1947. A simplified method of elastic-stability analysis for thin cylindrical shell. Tech. Rep. 874, NACA.

Black, J. T., Whetzal, J., deBlonk, B. J., Massarello, J. J., 2006. Deployment repeatability testing of composite tape springs or space optics applications. proceedings of the 47th AIAA/ASME/ASCE/AHS/ASC Structures, Structural Dynamics, and Materials Conference.

Carr, J., Gurtin, M., Slemrod, M., 1984. Structured phase transitions on a finite interval. Archive for Rational Mechanics and Analysis 86, 317–351.

Coleman, B. D., Newman, D. C., 1988. On the rheology of cold drawing. i. elastic materials. Journal of Polymer Science. Part B: Polymer Physics 26, 1801–1822.

Donzier, A., Sicre, J., 1997. Self actuating damped hinge. proceedings of the 7th European Space Mechanisms and Tribology Symposium.

Ericksen, J. L., 1975. Equilibrium of bars. Journal of elasticity 5, 191–201.

Ericksen, J. L., 1998. Introduction to the Thermodynamics of Solids. Vol. 131 of Applied Mathematical Sciences. Springer.

Guinot, F., Bourgeois, S., Cochelin, B., Blanchard, L., 2012. A planar rod model with flexible thin-walled cross-sections. application to the folding of tape springs. International Journal of Solids and Structures 49 (1), 73 – 86.

Hoffait, S., Bruls, O., Granville, D., Cugnon, F., Kerschen, G., 2010. Dy-

namic analysis of the self-locking phenomenon in tape-spring hinges. Acta Astronautica 66, 1125–1132.

Kyriakides, S., 1993. Propagating instabilities in structures. Advances in applied mechanics 30, 67–189.

ManLab-4.0, 2018. An interactive path-following and bifurcation analysis software. http://manlab.lma.cnrs-mrs.fr/, accessed: 2018-09-15.

Murphey, T., Jeon, S., Biskner, A., Sanford, G., 2010. Deployable booms and antennas using bi-stable tape springs. In: 24th Annual AIAA/USU Conference on Small Satellites.

Pellegrino, S., 2002. Crts reflectors. Tech. rep., Department of Engineering, Univeristy of Cambridge.

Picault, E., Bourgeois, S., Cochelin, B., Guinot, F., 2016. A rod model with thin-walled flexible cross-section: extension to 3D motions and application to 3D foldings of tape springs. International Journal of Solids and Structures 84, 64–81.

Picault, E., Marone-Hitz, P., Bourgeois, S., Cochelin, B., Guinot, F., 2014. A planar rod model with flexible cross-section for the folding and the dynamic deployment of tape springs: Improvements and comparisons with experiments. International Journal of Solids and Structures 51 (18), 3226 – 3238.

Puglisi, G., Truskinovsky, L., 2002. Rate independent hysteresis in a bi-stable chain. Journal of the mechanics and physics of solids 50, 165–187.

Rogers, R., Truskinovski, L., 1997. Discretization and hysteresis. Physica B 233, 370–375.

Seffen, K., Pellegrino, S., 1999. Deployment dynamics of tape springs. Proceedings of the Royal Society of London A 455, 1003–1048.

Seffen, K. A., You, Z., Pellegrino, S., 2000. Folding and deployment of curved tape springs. International Journal of Mechanical Sciences 42, 2055–2073.

Soykasap, O., 2012. Curved large tape springs for an ultra-thin shell deployable reflector. Journal of Reinforced Plastics and Composites 31, 691–703.

Truskinovsky, L., Zanzotto, G., 1996. Ericksen's bar revisited: energy wiggles. Journal of the mechanics and physics of solids 44, 1371–1408.

Walker, S. J. I., Aglietti, G., 2007. Modeling the hinge moment of skew mounted tape spring folds. Journal of Aerospace Engineering 20 (2), 102–115.

Wuest, W., 1954. Einige Anvendungen der Theorie der Zylinderschale. Z. Angew. Math. Mech. 34, 444–454.

Appendix A. Governing equations of the *RFleXS-2DS* model with arc-of-circle cross-section and estimate of the propagating fold moment $\hat{\boldsymbol{M}}^*$

Assuming that the cross-section remains an arc-of-circle after deformation, the model only involves one variable to describe the cross-section shape :

$$\hat{z} = \hat{\beta}^e(\hat{s}_1)\left(\frac{\hat{s}_2^2}{2} - \frac{1}{6}\right). \tag{A.1}$$

The expression (A.1) is introduced in the elastic potential energy (20) and (21), taking into account Eq. (12). The differentiation and integration by parts leads to the strong form of the equilibrium equations (with cross-sections at ends free to deform):

The uniform solution for which $\hat{\beta}^e$ and $\hat{k}^r = \hat{\theta}_{,1}$ do not depend on $\hat{s}_1$ and must verify:

$$\begin{aligned} &\left(\tfrac{4}{15}Z^2\hat{\beta}^{e^2}+1\right)\hat{k}^r - \nu\left(\hat{\beta}^e - 1\right) = \hat{M}, \\ &\tfrac{4}{15}Z^2\hat{\beta}^e\hat{k}^{r^2} - \nu\hat{k}^r + \hat{\beta}^e - 1 = 0. \end{aligned} \tag{A.2}$$

Solutions of this system (A.2) are

$$\hat{M} = \hat{k}^r - \nu(\hat{\beta}^e - 1) + \frac{4}{15}Z^2(\hat{\beta}^e)^2\,\hat{k}^r \qquad \text{with} \qquad \hat{\beta}^e = \frac{1+\nu\hat{k}^r}{1+\frac{4}{15}Z^2\hat{k}^{r^2}}. \tag{A.3}$$

Plots of $\hat{M}(\hat{k}^r)$ and $\hat{\beta}^e(\hat{k}^r)$ are shown in Figure 11 for the geometrical and material properties corresponding to Z=114.47. The estimate of the propagating fold moment $\hat{M}^* = 1+\nu$ proposed by Seffen and Pellegrino (1999) is reported in this Figure . It is shown in the following that the proposed model yields the same estimate. First, it must be noticed that for small curvature $\hat{k}^r$, the bending moment $\hat{M}(\hat{k}^r)$ is mainly governed by the rod overall bending because the second moment of area of the cross-section is high. On the contrary, for high curvature, the cross-section is almost completely flattened (see the plot $\hat{\beta}^e(\hat{k}^r)$ in Figure 11) and the bending moment is mainly governed by the local shell bending. It leads to simplify equations (25) for these two cases :

- for rod-dominated behaviour (relatively small curvature $\hat{k}^r$),

$$\hat{\beta}^e \approx \frac{1}{1+\frac{4}{15}Z^2\hat{k}^{r^2}} \qquad \text{and} \qquad \hat{M} \approx \frac{4}{15}Z^2\frac{\hat{k}^r}{\left(1+\frac{4}{15}Z^2\hat{k}^{r^2}\right)^2}, \tag{A.4}$$

- for shell-dominated behaviour (relatively high curvature $\hat{k}^r$),

$$\hat{\beta}^e \approx 0 \qquad \text{and} \qquad \hat{M} \approx \nu + \hat{k}^r. \tag{A.5}$$

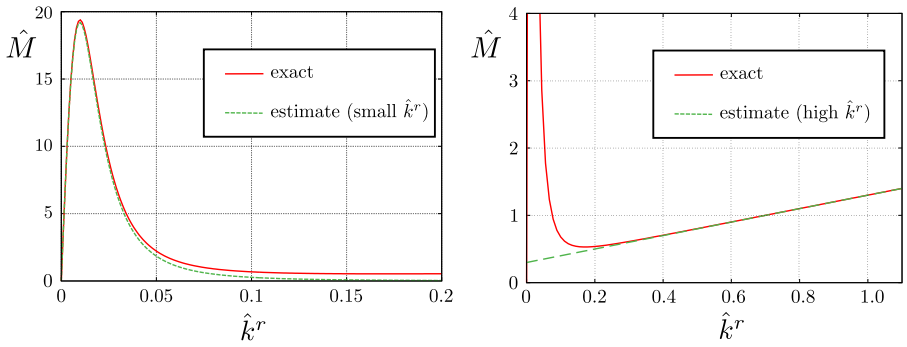

Figure A.25: Bending moment $\hat{M}(\hat{k}^r)$ and estimates for small and high longitudinal curvatures $\hat{k}^r$ for $Z = 114.47$.

The consistency of these approximations are illustrated in Figure A.25. The propagating fold moment $\hat{M}^*$ must verify (equality of areas A_1 and A_2 in Figure 11):

$$\int_{\hat{k}_1^{r^*}}^{\hat{k}_2^{r^*}} \hat{M}\,\mathrm{d}\hat{k}^r = \hat{M}^*(\hat{k}_2^{r^*} - \hat{k}_1^{r^*}) \quad \Rightarrow \quad \int_0^{\hat{k}_2^{r^*}} \hat{M}\,\mathrm{d}\hat{k}^r - \int_0^{\hat{k}_1^{r^*}} \hat{M}\,\mathrm{d}\hat{k}^r = \hat{M}^*(\hat{k}_2^{r^*} - \hat{k}_1^{r^*}), \tag{A.6}$$

with $\hat{k}_1^{r^*}$ and $\hat{k}_2^{r^*}$ the smallest and highest positive values of $\hat{k}^r$ verifying $\hat{M}(\hat{k}^r) = \hat{M}^*$. Using estimates (A.4) and (A.5) of $\hat{M}(\hat{k}^r)$ for small and high curvatures leads to:

$$\hat{M}(\hat{k}_1^{r^*}) = \hat{M}^* \approx \frac{4}{15} Z^2 \frac{\hat{k}_1^{r^*}}{\left(1 + \frac{4}{15} Z^2 \hat{k}_1^{r^2}\right)^2} \qquad \text{and} \qquad \hat{M}(\hat{k}_2^{r^*}) = \hat{M}^* \approx \nu + \hat{k}_2^{r^*}.$$

Furthermore, Figure 11 suggests to assume that

$$\hat{k}_2^{r^*} >> \hat{k}_1^{r^*} \text{ and } \int_0^{\hat{k}_2^{r^*}} \hat{M}\,\mathrm{d}\hat{k}^r >> \int_0^{\hat{k}_1^{r^*}} \hat{M}\,\mathrm{d}\hat{k}^r. \tag{A.7}$$

Finally, Equation (A.6) leads to $\int_0^{\hat{k}_2^{r^*}} \hat{M}\,\mathrm{d}\hat{k}^r \approx \hat{M}^* \hat{k}_2^{r^*} \approx (\hat{k}_2^{r^*} + \nu)\hat{k}_2^{r^*}$. Combining equations in (A.3) leads an expression of $\hat{M}(\hat{k}^r)$ that can be integrated. It leads to:

$$\int_0^{\hat{k}_2^{r^*}} \hat{M}\,\mathrm{d}\hat{k}^r = \frac{(\hat{k}_2^{r^*})^2\left(15(1-\nu^2)+4Z^2\left(1+\hat{k}_2^{r^*}(\hat{k}_2^{r^*}+2\nu)\right)\right)}{30+8Z^2(\hat{k}_2^{r^*})^2} \approx (\hat{k}_2^{r^*}+\nu)\hat{k}_2^{r^*}.$$

Assuming that $Z^2 >> 1$ and $\hat{k}_2^{r^*}$ of the order of unity (valid in practice), the solution of this last equation is $\hat{k}_2^{r^*} \approx 1$ and then $\hat{M}^* \approx 1+\nu$ and $\hat{k}_1^{r^*} \approx \frac{15}{4}\frac{1+\nu}{Z^2}$. These values make assumptions (A.7) valid and are in agreement with the estimates proposed by Seffen and Pellegrino (1999). In the fold area, the cross-section is almost completely flattened ($\beta^e \approx 0$) and the longitudinal curvature is close to the initial transverse curvature ($\hat{k}_2^{r^*} \approx 1$). The curvature $\hat{k}_1^{r^*} \approx \frac{15}{4}\frac{1+\nu}{Z^2}$ can be obtained with the linear classical beam theory for which the deformation of the cross-section is neglected. It is shown here that the assumption of arc-of-circle cross-section leads to the same estimate of the propagating fold moment $\hat{M}^* \approx 1+\nu$ obtained by Seffen and Pellegrino (1999).